International Journal of Thermal Sciences 221 (2026) 110466

Contents lists available at ScienceDirect

International Journal of Thermal Sciences

journal homepage: www.elsevier.com/locate/ijts

Analytical solution and parametric design of bio-PCM-based passive BTMS for cylindrical lithium-ion cells under lumped model assumptions

A. Afass [a,*], S. Landini [b], O. Elghaz [c], B. Lamrani [c], T. Kousksou [a]

[a] *Université de Pau et des Pays de L'Adour, E2S UPPA, SIAME, Pau, France*
[b] *School of Engineering, Mathematics and Physics, University of East Anglia, Norwich, NR4 7TJ, United Kingdom*
[c] *Mohammed V University in Rabat, Faculty of Sciences, MANAPSE Laboratory, 1014, RP, Rabat, Morocco*

ARTICLE INFO

Keywords:
Li-ion cells
Bio-based PCM
Analytical thermal model
Battery thermal management
Parametric analysis
Driving cycles

ABSTRACT

The present study proposes a parametric investigation of a passive battery thermal management system (BTMS) utilizing bio-based phase change materials (bPCMs). The thermal network approach allocates to the cell and the bPCM two thermal nodes to accurately capture the surface and core temperatures of the cell as well as the two concentric layers of the bPCM. A novel analytical solution to the thermal network model is introduced for the first time in the context of cell-bPCM configuration. The resolution is implemented through the zero-order hold discretisation technique, which involves piecewise time integration. Validation against experimental and computational fluid dynamics data under variable load demonstrates the model's predictive capability. Notably, this work features an extensive parametric analysis, examining both bPCM and cell thermo-physical parameters, thereby providing new insight into their effects on thermal performance over consecutive charge-discharge cycles. Results indicate that a 6 mm bPCM layer thickness was identified as optimal, providing a balance between thermal performance and system compactness. A lower melting point within the operating range leads to earlier activation of latent thermal absorption. The heat of fusion showed diminishing benefits beyond 200 kJ/kg, while bPCM thermal conductivity mainly improved internal homogeneity rather than peak suppression. Variations in bPCM density showed negligible impact on peak cell temperature but influenced thermal storage capacity. Furthermore, the study encompasses the effects of battery format, where the cell radius was found to be inversely proportional to temperature spikes observed, while cells with higher heat capacity showed improved resilience to thermal spikes. Notably, increasing the ambient heat transfer coefficient from 5 to 100 $W/m^2.K$ significantly enhances heat dissipation to the environment and promotes thermal recovery of the bPCM between cycles, reducing peak cell temperatures by up to 3 °C. Additionally, analysis of the BTMS under realistic driving conditions (WLTC, JC08, CLTC, NEDC, UDDS) underscores the system's ability to maintain the cell operating temperature within its optimal range ($<$36.2 °C), with temperature differences below 6 °C across all driving scenarios examined. This work provides a scalable tool for BTMS design and sizing, facilitating the integration of sustainable solutions into electric vehicles.

1. Introduction

Li-ion batteries (LIBs) are considered one of the key solutions for reducing the carbon footprint of the global transport sector [1]. However, a number of obstacles and challenges need to be overcome before these technologies can be deployed on a large scale. These challenges include technological [2], geopolitical [3], economic [4], environmental [5] and societal factors, particularly in terms of acceptability and social justice [6,7]. In other words, LIBs should simultaneously achieve high energy density, optimal safety, reasonable cost, and low environmental impact [8,9]. However, meeting all of these criteria simultaneously is a significant challenge, as they are often interrelated and may conflict with one another, complicating their optimisation.

In terms of safety, thermal runaway is one of the main technological challenges facing the integration of LIB in electric vehicles [10,11]. This phenomenon arises from the excessive generated heat, which degrades the solid electrolyte interphase, triggering a self-sustained reaction that leads to further heat generation, potentially causing fire or explosion

---

This article is part of a special issue entitled: Battery Thermal Management published in International Journal of Thermal Sciences.

* Corresponding author.
E-mail address: aafass@univ-pau.fr (A. Afass).

https://doi.org/10.1016/j.ijthermalsci.2025.110466
Received 20 August 2025; Received in revised form 23 October 2025; Accepted 6 November 2025

Table 1
Summary of published method related to solving thermal model of LIB.

Authors	Paper scope	Solving approach method
[47]	Investigate the performance of single-phase forced immersion cooling in Li-ion batteries	COMSOL based solver
[48]	Utilizing supercritical CO_2 as a direct-contact coolant for cylindrical Li-ion cells	Finite Volume Method Ansys solver
[49]	Analysing the thermal performance of a passive BTMS of a battery pack of 24 cells	Numerical based approaches for lumped thermal model
[44,50]	Assessing the impact of cell designs and thermal management approaches on the internal temperature. cell designs and cooling approaches and their effects on the internal temperature of the cell.	Finite difference Crank-Nicolson to solve a 3D distributed thermal network model.
[45]	Elucidating the effect of PCM passive BTMS influence on the temperature distribution in LIB.	Iterative semi-analytical approach based on the Eigenfunction expansion and perturbation method.
[46]	Unidimensional analytical solution in Cartesian and cylindrical coordinates for LIB surrounded by PCM.	Analytical solution for unidirectional heat transfer equation
[51]	Compare zero and first order Hermite integral approximations of lumped capacitance model to Green function solution of cylindrical cell.	Analytical solution for unidirectional heat transfer equation
[39]	Verifying experimentally the accuracy of analytical solution of distributed thermal model for Tesla batterie pack.	Analytical solution of lumped thermal model
[52]	Modelling closed loop liquid cooling batterie pack with distributed thermal network model.	Analytical solution of lumped thermal model

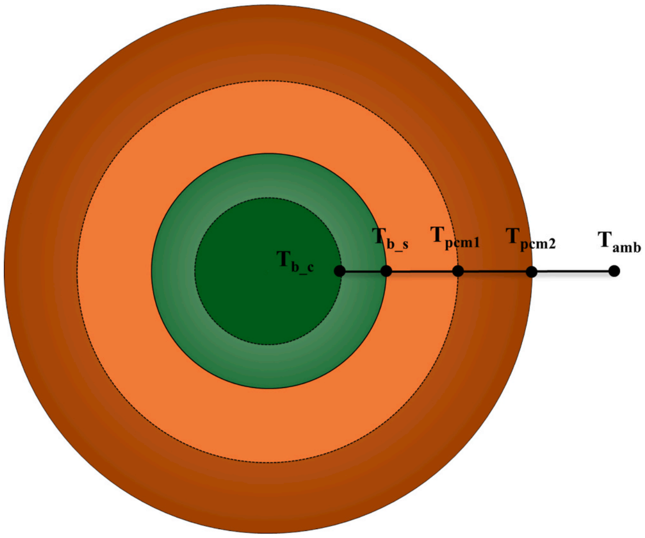

Fig. 1. Radial cross-section of the battery- PCM system, showing battery (green) core temperature (T_{b_c}), and surface (T_{b_s}), the two bPCM (orange) zones (T_{pcm1}, T_{pcm2}), and ambient temperature (T_{amb}).

[12]. Such an incident represents a critical risk to the safety of users and to the battery's longevity, demanding a robust battery thermal management system (BTMS) [13]. However, the integration of a BTMS has a substantial impact on the performance of both the battery and the electric vehicle [14,15]. Therefore, it is essential to optimise its design, size, and weight to ensure smooth integration without compromising its overall energy efficiency. The design must carefully consider the potential effects on vehicle performance while maintaining a suitable compromise between various criteria [16].

In recent years, various approaches based on passive, active, or hybrid systems have been proposed and extensively studied in the literature for the thermal management of LIB [17–19]. Each of these solutions has its advantages and disadvantages. Phase change material (PCM) stands out from all the passive solutions for BTMS that have emerged in recent years [18,19]. One of its main advantages is that it offers excellent thermal uniformity in a passive way, while being based on a simple structure. The versatility of PCM as passive thermal management systems has led to their adoption across various disciplines, from electronics to sustainable design buildings [20]. Paraffin, as a PCM, is widely used by researchers because of its many advantages, including its low cost, resistance to decomposition and ability to operate at optimum temperatures [21,22]. These factors help prevent thermal runaway and ensure efficient thermal management.

All PCMs reviewed in the literature have relatively low thermal conductivity, lying between 0.15 and 0.42 W m^{-1} K^{-1} [23–26], which limits their effectiveness in dissipating heat, particularly during consecutive charge and discharge cycles and/or at high current rates, even though these solutions often result in a decrease in the latent heat of PCM [27,28].

A key challenge in implementing a PCM-based BTMS is minimising its carbon footprint. In this regard, bio-sourced based phase change materials (bPCM) offer a potential solution [29–31]. However, several drawbacks must be addressed to ensure their effectiveness in the electric mobility context, including the large-scale accessibility of these materials, the necessity to decrease production costs, the mitigation of the material's rate of ageing, and the prevention of its performance decline. bPCMs are often cheaper when sourced from waste oils or animal fats, with a price around 1.3–1.77 (US$/kg), compared to paraffin wax with a price range between 1.87 and 2 (US$/kg). Although the paraffins are more chemically stable and endure long-term usage (+1000 cycles), they pose a greater fire risk. On the other hand, bPCMs are safer and environmentally preferable, with a slight decline in performance over time. Additional challenges involve the high supercooling phenomenon, which prevents the transition from liquid to solid phase [32]. Fire resistance is also a critical aspect, where researchers are focusing on methods aimed at reinforcing its resistance, ensuring the safety of BTMS using PCMs [33]. The composite PPCTH2 developed by Li *et al.* [33] significantly reduces peak heat release under cone calorimeter tests (heat release rate, total heat release, smoke production). In addition, during the flammability test, the PPCTH2 was ignited for 30 s with a flame spray gun, then it self-extinguished within 1 s after the ignition source was removed. Palm oil as a bPCM was investigated by Fabiani *et al.* [34]. The palm oil was found to be stable after 10000 cycles with a reduction in latent heat of 21 %, with a 1 °C deviation regarding the onset melting temperature. The life cycle assessment of this bPCM is very similar to commercial paraffin if palm oil is regarded as a raw material. Owning to the significant environmental impact associated with deforestation, land use, and emissions from transportation and cultivation. However, when palm oil is evaluated as a waste stream, its environmental footprint is much lower than paraffin. Furthermore, accurate thermophysical characterisation of bPCM is mandatory for physical modelling, numerical simulation, sizing, and optimisation.

A dynamic thermal model of LIB is essential to evaluate the performance of the BTMS in mitigating temperature changes during charge and discharge cycles. Several modelling approaches were proposed in the literature, each with different levels of accuracy and complexity [35–37]. Among these, Computational Fluid Dynamics (CFD) is recognised for its high fidelity and detailed spatial resolution, but it remains computationally expensive, making it less suitable for extensive parametric analyses or real-time applications like BTMS monitoring and digital twinning [38].

To tackle these constraints, researchers explored straightforward and

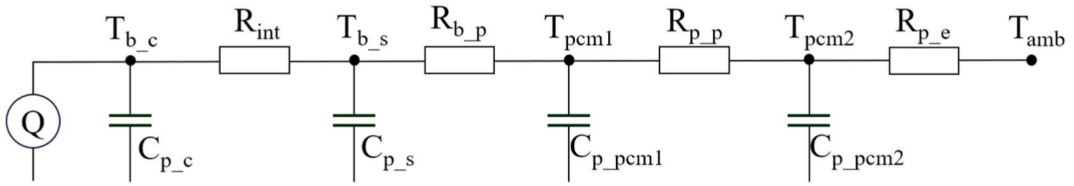

Fig. 2. Lumped thermal network model of the battery-bPCM system.

Table 2
Thermo-physical properties of bPCMs evaluated.

PCM properties	Specific heat capacity (Cp) (J/kg.K)	Latent heat (kJ/kg)	Thermal conductivity (W/m.K)	Density (kg/m^3)	Solidus temperature (°C)	Liquidus temperature (°C)
Capric acid [59–61]	2100 – 1900	139.77–168.77	0.153–0.19	1004 878	25.57–28.85	29.62–32.15
Composite eutectic PCM [61]	N/A	158.32	0.726	N/A	N/A	37.03
Beef tallow [62]	2250	86.6	0.174	945 (solid) 846 (liquid)	30	33
Allanblackia [63]	N/A	80.53	N/A	N/A	30.5	34.74–37
Composite bio-based polyethylene glycol [64]	N/A	74.3	10.83	N/A	33.15	34.51
Palmitic acid [65]	2059,4 (solid) 2267 (liquid)	203.4	0.162 (solid) 0.159 (liquid)	989 (solid) 850 (liquid)	53	65
Stearic acid [65]	2830 (solid) 2380 (liquid)	186.5	0.180	1080 (solid) 1015 (liquid)	24.5	69.5
Coconut oil [66]	3750 2010	105	0.228 0.166	920 914	15	32
The range covered in this study [67]	1500	50–280	0.1–5	700–1400 (solid) 860-1400 (liquid)	29–35	34–40

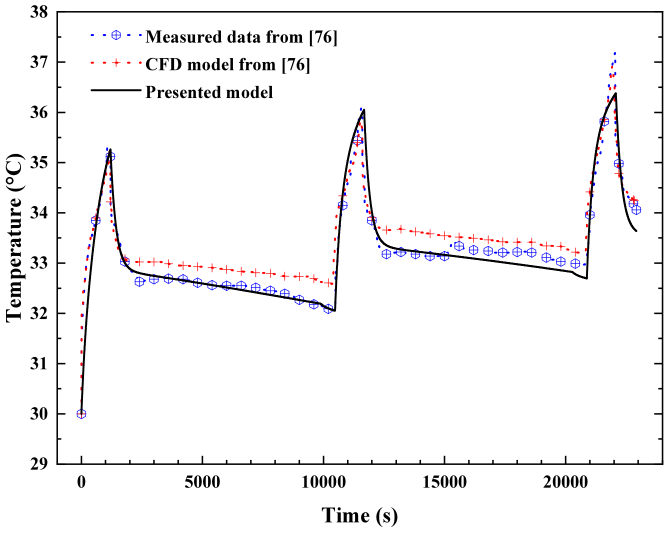

Fig. 3a. Validation of the lumped thermal model against experimental data [76] and CFD results for a 3C discharge current and 0.5C charge current.

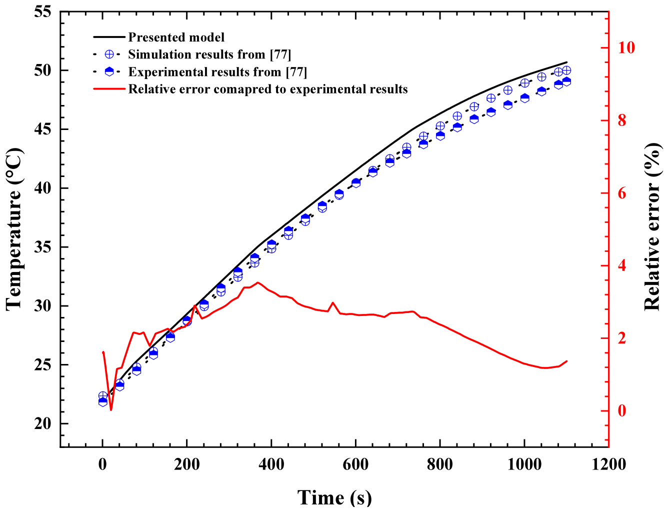

Fig. 3b. Validation of battery surface temperature profile against experimental data and CFD results [77].

simpler options for complex models. For instance, White *et al.* [39] proposed a thermal network model to estimate temperatures in the unmonitored zone for the Tesla Model 3 SR + battery pack. Their spatially extrapolated temperature sensors methodology offers a highly efficient alternative to CFD for real-time thermal monitoring. Similarly, an analysis contrasted the lumped-capacitance model with the Newman-Tiedemann-Gu-Kim (NTGK) CFD-based approach for forecasting battery surface temperature across different discharge loads [40]. The investigation demonstrated that the lumped model attained similar predictive accuracy for battery surface temperature across the examined scenarios. The lumped model achieves the simulation of the HWFET driving cycle in under 8 s, a stark contrast to the 7 h needed by the NTGK model.

Lumped modelling has also proven effective for the parametric analysis of PCM-based BTMS. Studies such as Lebrouhi *et al* **[**41**]** and Lamrani *et al.* [42] illustrate the practicality of these models for BTMS sizing under various scenarios. However, their limited ability to capture spatial temperature variations has led to growing interest in more advanced thermal models like the two-state thermal model [43] or the distributed equivalent circuit network model [44].

Correspondingly, effort in refining the numerical solutions to these models gives rise to analytical modelling, which is a powerful tool for the rapid design and evaluation of PCM-based BTMS. Parhizi and **Jain**

Table 3
Default and range value of battery and bPCM parameters.

Parameters	Unit	Default value	Parametric study range
bPCM layer width	(m)	0.006	0. 0001–0.012
bPCM melting temperature (solidus/liquidus)	(°C)	29/34	25/30–35/40
Specific heat capacity of bPCM	(J/kg. K)	1500	N/A
Density of bPCM	(kg/m^3)	860	700–1400
bPCM thermal conductivity	(W/m. K)	0.2	0.1–5
bPCM latent heat	(kJ/kg)	198.050	50–280
Interfacial heat transfer coefficient	(W/m^2. K)	50	5–100
Cell height	(m)	0.0709	0.065–0.095
Cell diameter (m)	(m)	0. 0217	0.018–0.046
Call electrical capacity	(Ah)	4	N/A
Cell nominal voltage	(V)	3.6	N/A
Cell heat capacity	(J/kg. K)	1048	700–2000
Cell mass	(kg)	0.069	N/A
Cell radial thermal conductivity	(W/m. K)	1.19	0.1–5
Ambient convective heat transfer coefficient	(W/m^2. K)	5	5–100

[45] introduced an iterative analytical model, addressing the coupled heat transfer problem between the battery and surrounding PCM in one dimension. Their study relied on the perturbation method to reveal the limitations of PCM cooling in mitigating core temperatures and pointed out the necessity of enhancing the cell's thermal conductivity. Similarly, Kermani *et al.* [46] presented an exact analytical solution for heat transfer inside a cylindrical cell wrapped in PCM. By considering only the radial component, the model was used for precise estimation of optimal PCM thickness at different discharge currents. Overall, a detailed analytical solution relying on the perturbation method, Green function, Hermite integration approximations or Paterson's method provides exact solutions with high numerical complexity and computational resources. This complexity increased rapidly when the model considered a hybrid BTMS or three-dimensional aspects of the system. Hence the need for a balanced thermal approach with potential extension in three dimensions for ease. Table 1 summarises the other existing approaches to solving the BTMS thermal model.

In this paper, we presented and validated a new lumped capacitance model to describe the performance of a cylindrical LIB integrating a layer of bPCM. The spatial accuracy depends on the number of thermal nodes employed, while time resolution is ensured through the proposed piecewise analytical time integration, which is based on zero-order hold (ZOH) discretisation. Despite the numerical formulation simplicity, this approach captures the dynamic thermal behaviour of BTMS with high accuracy and minimal computational resources. The impact of the major geometric parameters, as well as the thermophysical properties of the

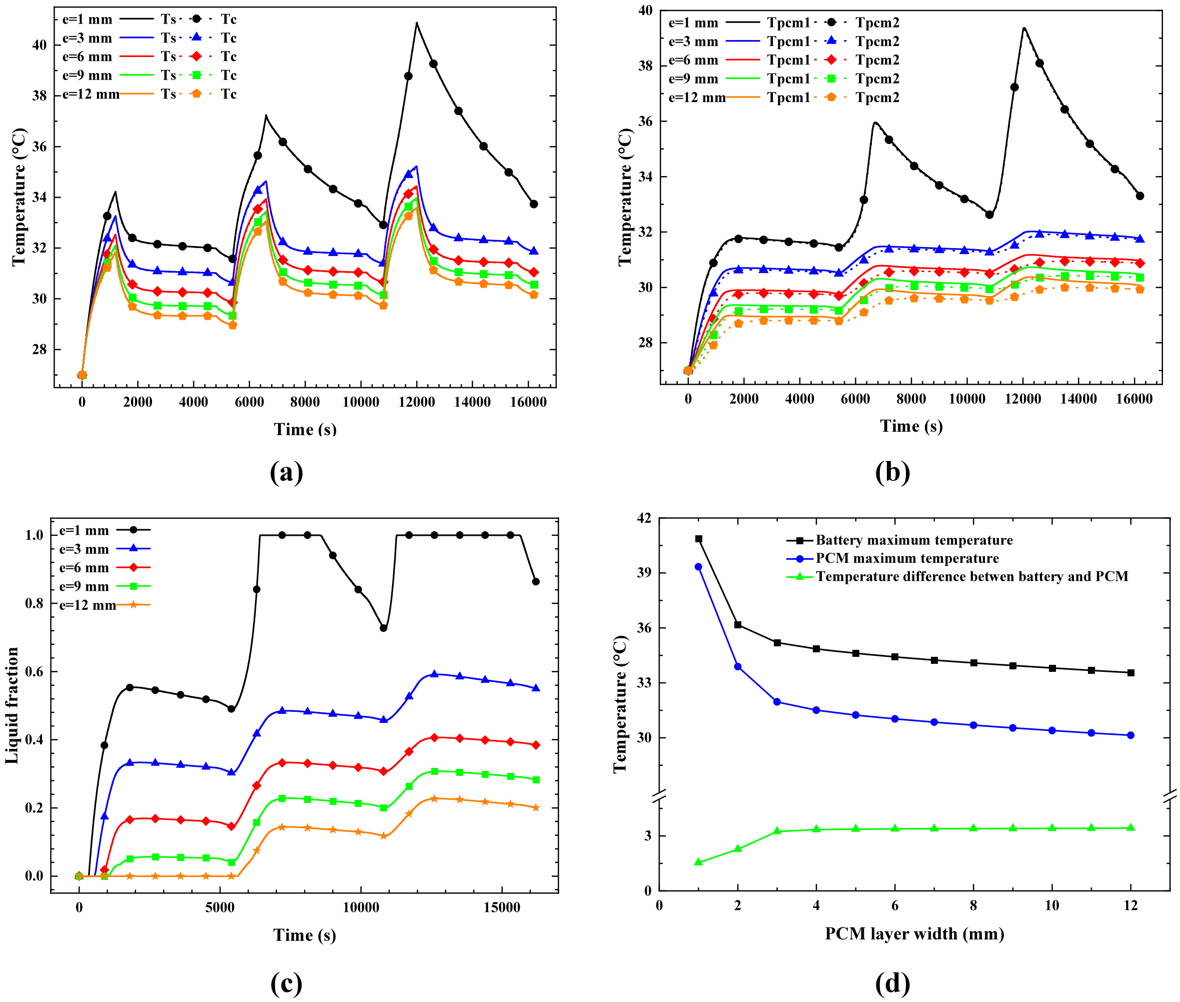

(a) (b)

(c) (d)

Fig. 4. Effect of bPCM layer thickness on (a) Battery core and surface temperature, (b) Temperature distribution in bPCM zones 1 and 2, (c) Global liquid fraction, (d) Maximum battery and bPCM temperatures.

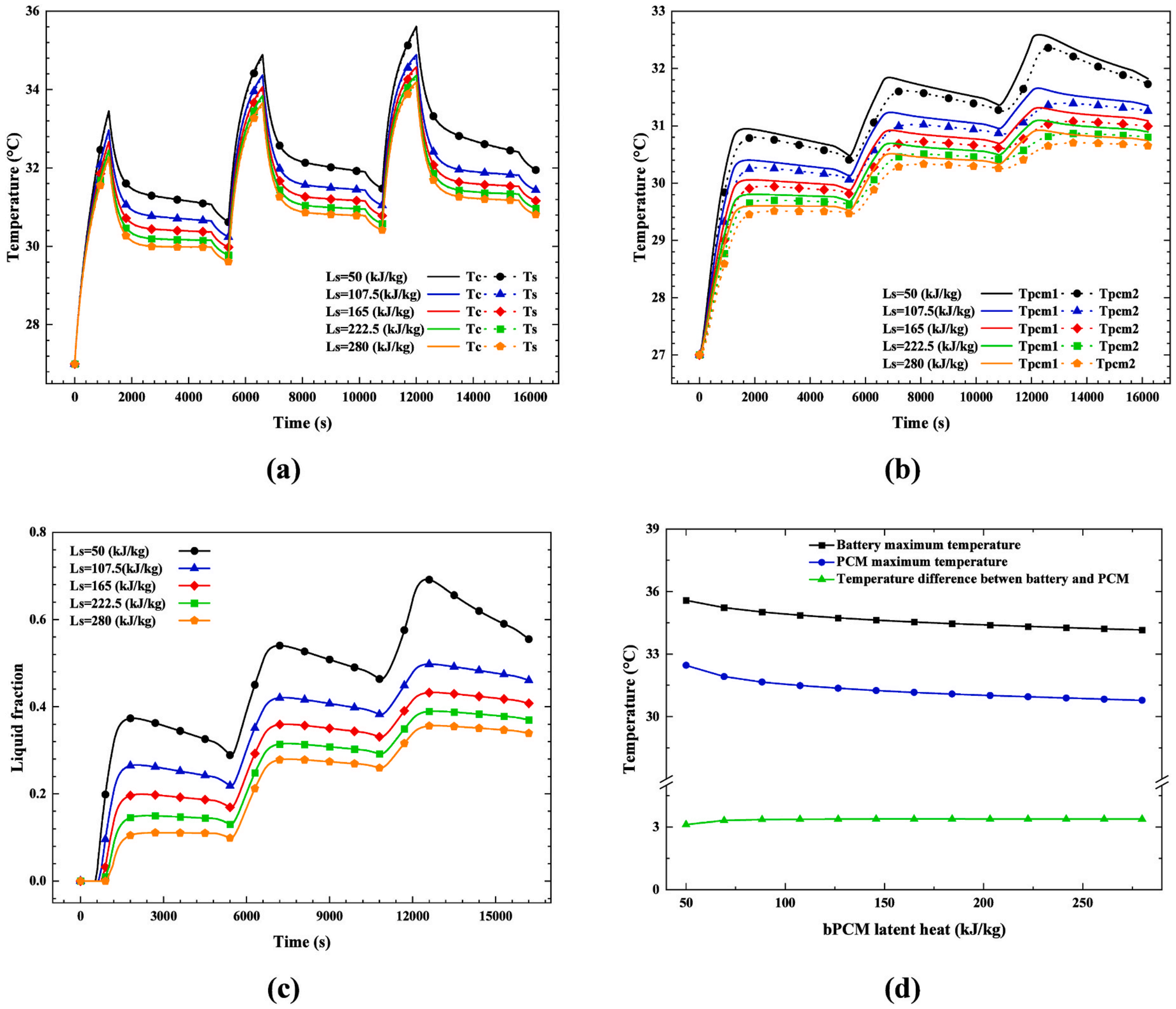

Fig. 5. Effect of bPCM latent heat on (a) Battery core and surface temperature, (b) Temperature distribution in bPCM zones 1 and 2, (c) Global liquid fraction, (d) Maximum battery and bPCM temperatures.

cell and the bPCM, were also presented and thoroughly investigated in this work. The proposed model could serve as a dynamic and scalable tool to assist in the design, sizing and optimisation of passive BTMS. It can also be used by engineers to quantify the influence of the thermophysical properties of cells and bPCM on critical thermal criteria, such as maximum temperature and internal thermal gradients inside the system.

This paper is structured as follows: Section 3 describes the BTMS components and their corresponding numerical models. Section 4 introduces the model's validation. Section 5 presents and discusses the parametric analysis of the BTMS. Ultimately, the conclusion highlights the key findings and the potential future directions.

2. Methodology

2.1. Physical model

The proposed BTMS consists of a battery encased in a bPCM layer, as seen in Fig. 1. The passive BTMS depends on the capacity of bPCM to retain significant amounts of heat during phase transition at nearly constant temperature. The average reported value for cell axial thermal conductivity is 21 (W m^{-1} K^{-1}), which **is** higher than the average radial one with a value of 1.2 (W m^{-1} K^{-1}) [53]. Hence, the thermal gradient along the axis is negligible when compared to the radial component [54]. Therefore, the physical model can be simplified to a unidirectional heat transfer problem. The battery domain is characterised by two thermal nodes representing the core (T_{b_c}) and the surface temperature (T_{b_s}). Similarly, the PCM layer is divided into two zones; in each one, the temperature is considered homogeneous and represented by thermal nodes (T_{pcm1}) adjacent to the battery surface and (T_{pcm2}) adjacent to ambient.

Upon disassembling a cylindrical Li-ion battery from the inside outward, one will encounter the hollow core, the spirally wrapped "jellyroll" layer, and the outer casing at the ends. Subsequently, the diameter of the jelly roll, which is the active material, can be deduced as follows $d_{jelly} = d_{cell} - d_{core} - 2t_c$. The thickness of the hollow core and the metallic case **is** a linear function of cell diameter, as indicated $d_{core} = 3.75\,mm + 0.05(d_{cell} - 21)$ and $t_{case} = 0.25\,mm + 0.01(d_{cell} - 21)$ [55,56]. A recent teardown investigation of the Tesla 4680 cylindrical cell found that the thickness of the nickel-plated steel case is 0.4 mm. This thick container provides sufficient rigidity to withstand internal pressure fluctuations during cycling and external mechanical stresses

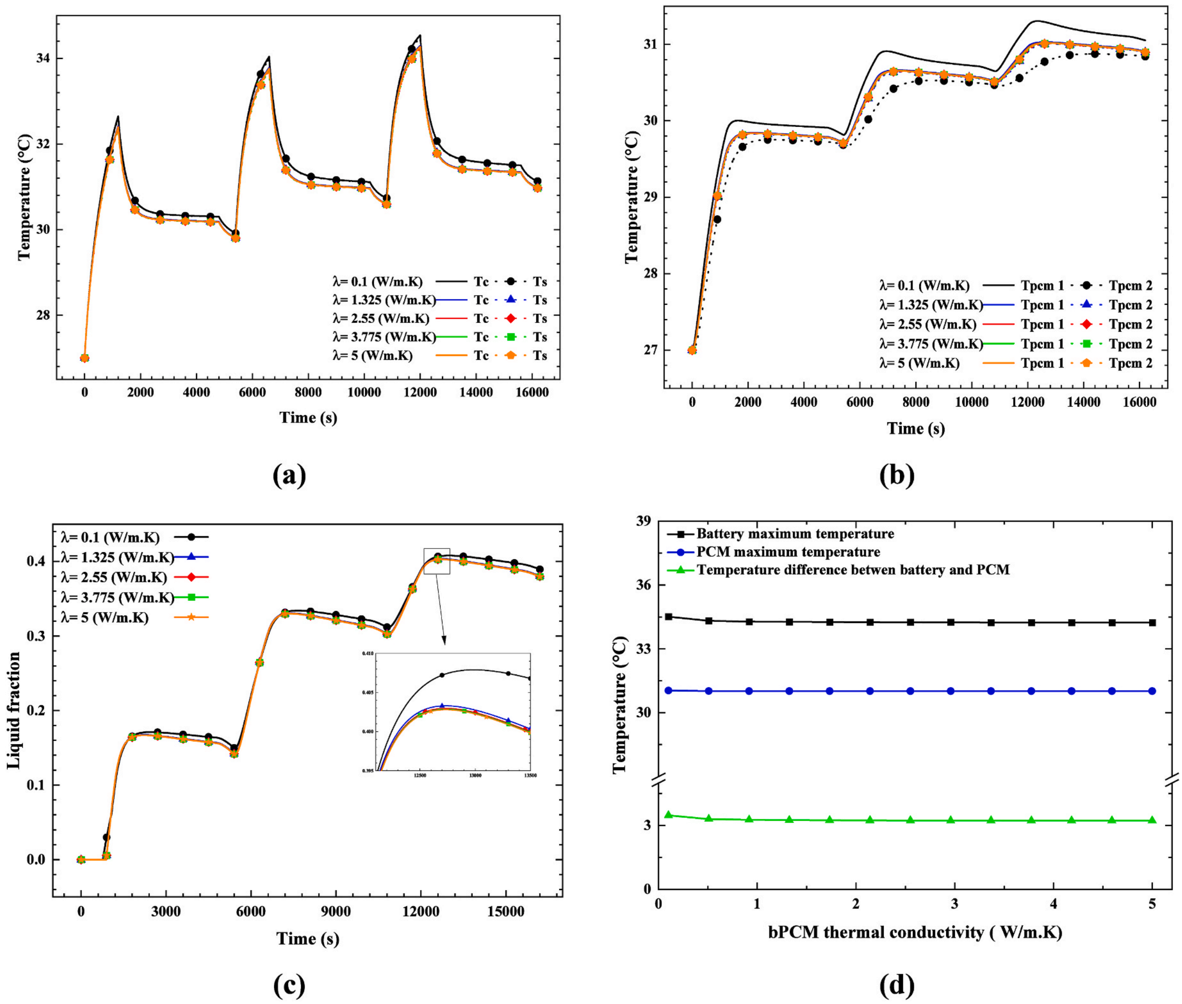

Fig. 6. Effect of bPCM thermal conductivity on (a) Battery core and surface temperature, (b) Temperature distribution in bPCM zones 1 and 2, (c) Global liquid fraction, (d) Maximum battery and bPCM temperatures.

from vehicle operation. [57]. The broad results measurement made it difficult to set a common value for cell measurement components. For simplicity's sake, in this study the battery core zone is characterised by a constant ratio of the core radius to the battery radius d_{core}/d_{cell}, maintained at 0.92, while the hollow core is neglected. The electrochemical reaction generates heat within the core region, then heat propagates in the battery and bPCM to the ambient. Due to the small width of the PCM layer compared to the height, the conductive heat transfer mode dominates the heat transfer in the PCM. With an aspect ratio (AR) of 3.875, the conduction accounts for more than 54 %–78 % of the average heat transfer, depending on the temperature gradient imposed and PCM thermophysical characteristics. Therefore, this study solely considers conductive heat transfer [58]. The proposed thermal network, as illustrated in Fig. 2, accommodates conductive heat transfer within the bPCM and battery, while radiant heat transfer is negligible. Both the density and thermal conductivity of bPCM, in solid and liquid phases, are assumed to be constant. However, during the phase transition (between the liquidus and solidus temperatures), an average value is employed. The effective heat capacity approach is used to describe the heat capacity value during phase transition in the bPCM **(**see Eq. (11)**).**

Additional assumptions have been adopted to model the phase transition of bPCM during charge and discharge cycles. These include omitting volume changes in bPCM during melting and solidification, as well as disregarding the phenomenon of supercooling, despite its potential impact on the material's thermal behaviour. These simplifications aim to reduce the complexity of the physical model while maintaining the accuracy required for simulation**.** The thermo-physical parameters of bPCM addressed in this study are listed in Table 2, with key materials including capric acids, composite eutectics, and bio-polyethylene glycol (PEG)-cellulose composites.

2.2. Governing equations

2.2.1. Battery thermal modelling

Based on the assumptions outlined above, the transient thermal battery response for cylindrical cells is modelled via the two-mass lumped thermal model, as represented in Fig. 2 [68].

$$m_c C_{p\_c} \frac{dT_{b\_c}}{dt} = Q + \frac{T_{b\_s} - T_{b\_c}}{R_{\text{int}}} \tag{1}$$

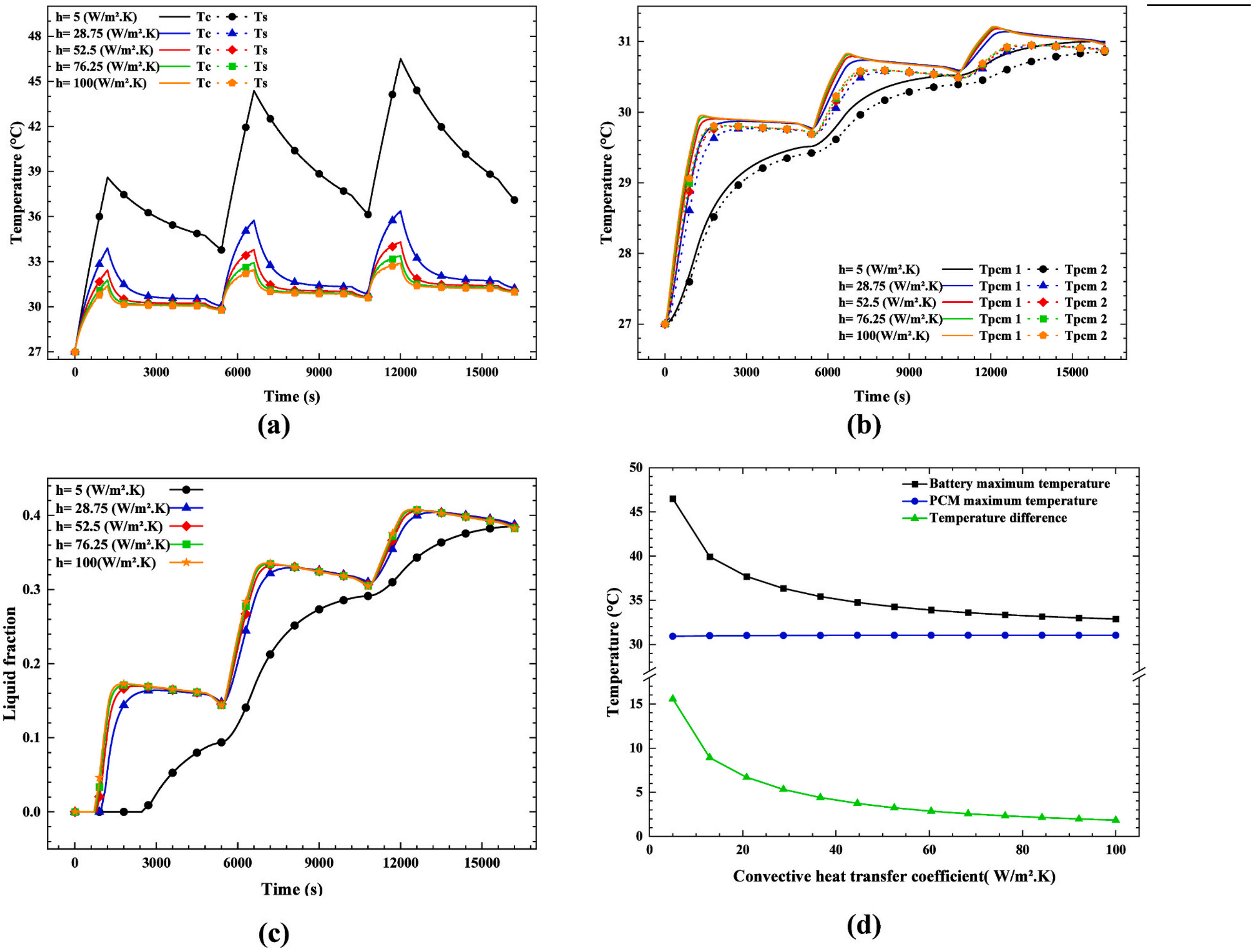

Fig. 7. Effect of interfacial heat transfer coefficient between bPCM and cell on (a) Battery core and surface temperature, (b) Temperature distribution in bPCM zones 1 and 2, (c) Global liquid fraction, (d) Maximum battery and bPCM temperatures.

$$m_s C_{p\_s}\frac{dT_{b\_s}}{dt}=\frac{T_{b\_c}-T_{b\_s}}{R_{\text{int}}}+\frac{T_{pcm1}-T_{b\_s}}{R_{b\_p}} \tag{2}$$

$$Q=RI^2 \tag{3}$$

Where m_c and m_s represent the mass of the battery core and surface. C_{p_c}, C_{p_s} are the heat capacities of the battery core and surface. Q is the heat generated in the battery core, with R being the total equivalent electrical resistance. Previous studies highlight the interplay between reversible and irreversible heat generation an under wide range of C-rate, they confirm that the reversible heat contribution to total heat generation under high C-rate is negligible, particularly under high C-rate [69–71]. The intricate heat generation term can be simplified to the irreversible heat generation component under high C-rates [72]. The thermal resistances R_{int} and R_{b_p} are defined as:

$$R_{\text{int}}=\frac{\ln\left(R_b/R_c\right)}{2\pi h_b k_b} \tag{4}$$

$$R_{b\_p}=\frac{1}{h_{b\_p}S_b} \tag{5}$$

Core and battery radius is denoted R_c and R_b, the battery height is h_b and the radial conductivity of the battery is k_b. The convective heat transfer coefficient in bPCM is h_{b_p} and the surface of the battery is S_b.

2.2.2. PCM thermal modelling

Based on the assumptions made, heat transfer coupled with phase transition in the PCM, is governed by the following equations:

$$m_{pcm1} C_{p\_pcm1}\frac{dT_{pcm1}}{dt}=\frac{T_{b\_s}-T_{pcm1}}{R_{b\_p}}+\frac{T_{pcm2}-T_{pcm1}}{R_{p\_p}} \tag{6}$$

$$m_{pcm2} C_{p\_pcm2}\frac{dT_{pcm2}}{dt}=\frac{T_{pcm1}-T_{pcm2}}{R_{p\_p}}+\frac{T_{amb}-T_{pcm2}}{R_{p\_e}} \tag{7}$$

Where m_{pcm1} and m_{pcm2} are the mass of the PCM in zone 1 and 2. The conductive R_{p_p} and convective R_{p_e} thermal resistances are defined as:

$$R_{p-p}=\frac{\ln\left(R_p/R_{ip}\right)}{2\pi h_b k_p} \tag{8}$$

$$R_{p-e}=\frac{1}{h_{p-amb}S_{amb}} \tag{9}$$

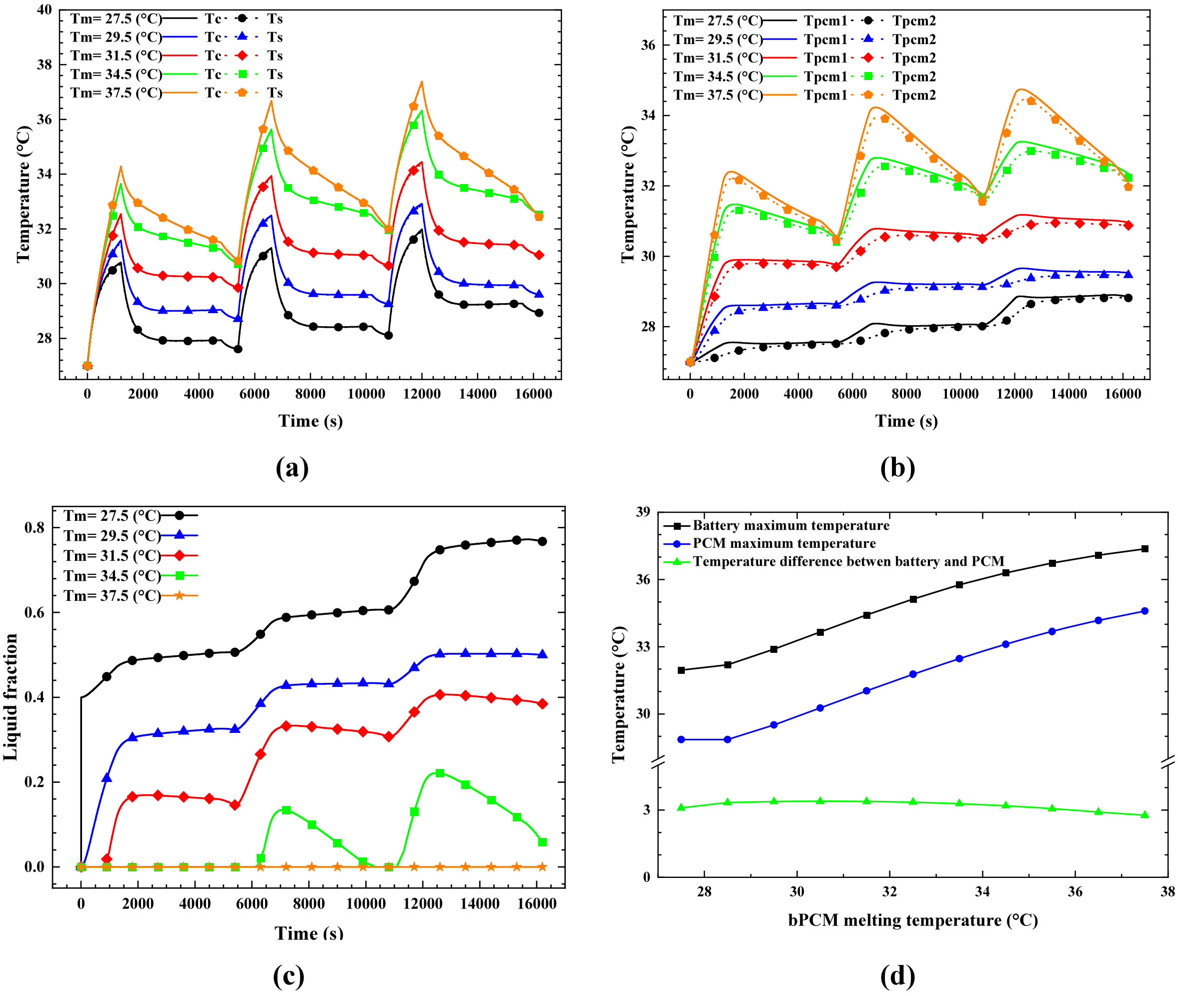

Fig. 8. Effect of melting temperature point of bPCM on (a) Battery core and surface temperature, (b) Temperature distribution in bPCM zones 1 and 2, (c) Global liquid fraction, (d) Maximum battery and bPCM temperatures.

R_p denotes the radius of the bPCM and the battery, while R_{ip} is the radius of the battery and half bPCM layer. S_{amb} is the outer surface of the system.

The solid-liquid phase transition of bPCM is modelled via the effective heat capacity method, where the effective heat capacity contains sensible and latent heat capacity [42,73]:

$$C_{pcm}(T) = C_{sensible}(T) + C_{latent}(T) \tag{10}$$

The specific heat capacity of the liquid and solid phases is set apart by:

$$C_{sensible}(T) = f(T)C_s(T) + (1 - f(T))C_l(T)$$

And the effective heat capacity is defined through the variation of the liquid fraction [74]:

$$C_{latent}(T) = Ls\frac{\partial f(T)}{\partial T} \tag{11}$$

Where, L_s is the latent heat of fusion, and *f(T)* represents the liquid fraction function, ranging from 0 to 1, defined as:

$$f(T) = \frac{1}{\pi}\left[\arctan\left(\frac{2\gamma(T - T_m)}{T_l - T_s}\right) + \frac{\pi}{2}\right] \tag{12}$$

T_l and T_s are the temperatures of liquid and solidus, γ is the dimensionless inclination set as 3.1. Finally, the effective heat capacity of the bPCM is expressed as a function of temperature as follows [75]:

$$C_{pcm}(T) = C_{sensible}(T) + L_s\frac{\frac{2\gamma}{\Delta T}}{\pi\left(\left((T - T_m)\left(\frac{2\gamma}{\Delta T}\right)\right)^2 + 1\right)} \tag{13}$$

2.2.3. Analytical solution

The proposed coupled thermal network model employs a state-space approach to solve the coupled system of ordinary differential equations (ODEs) governing heat transfer in the battery and bPCM layers. The governing heat transfer Eq. (1) **(2) (6) (7)** are linearised and expressed in matrix form as:

$$\frac{d\mathbf{T}}{dt} = \mathbf{A}.\mathbf{T} + \mathbf{B} \tag{14}$$

Where the temperature vector T compasses the four temperatures of the system as follows:

$$\mathbf{T}(t)=\begin{bmatrix} T_c(t) \\ T_s(t) \\ T_{pcm1}(t) \\ T_{pcm2}(t) \end{bmatrix} \tag{15}$$

A is a 4 × 4 matrix of thermal resistance coefficients contains:

$$\mathbf{A}=\begin{bmatrix} \frac{-1}{m_c C_{p\_c} R_{\text{int}}} & \frac{1}{m_c C_{p\_c} R_{\text{int}}} & 0 & 0 \\ \frac{1}{m_s C_{p\_s} R_{\text{int}}} & -\left(\frac{1}{m_s C_{p\_s} R_{\text{int}}}+\frac{1}{m_s C_{p\_s} R_{b\_p}}\right) & \frac{1}{m_s C_{p\_s} R_{b\_p}} & 0 \\ 0 & \frac{1}{m_{pcm1} C_{p\_pcm1} R_{b\_p}} & -\left(\frac{1}{m_{pcm1} C_{p\_pcm} R_{b\_p}}+\frac{1}{m_{pcm1} C_{p\_pcm} R_{p\_p}}\right) & \frac{1}{m_{pcm1} C_{p\_pcm} R_{p\_p}} \\ 0 & 0 & \frac{1}{m_{pcm2} C_{p\_pcm} R_{p\_p}} & -\left(\frac{1}{m_{pcm2} C_{p\_pcm} R_{p\_p}}+\frac{1}{m_{pcm2} C_{p\_pcm} R_{p\_e}}\right) \end{bmatrix} \tag{16}$$

B is a vector includes the rest terms of the equations system.

$$\mathbf{B}=\begin{bmatrix} \frac{Q}{m_c C_{p\_c}} \\ 0 \\ 0 \\ \frac{T_{amb}}{m_{pcm2} C_{p\_pcm} R_{p\_e}} \end{bmatrix} \tag{17}$$

To solve this system, an analytical piecewise approach is adopted. Within each time step Δt, matrices **A** and **B** values are constant, and their values are updated dynamically over each time step enabling a recursive solution over a time step:

$$\mathbf{T}(t+\Delta t)=e^{\mathbf{A}\Delta t}.\mathbf{T}(t)+\mathbf{A}^{-1}.\left(e^{\mathbf{A}\Delta t}-\mathbf{I}\right).\mathbf{B} \tag{18}$$

The presented approach inherently avoids stability limitations associated with explicit Euler or Runge-Kutta schemes, particularly if fast parameter fluctuations or disparate thermal time constants are present. The piecewise constant method allows the model to contain time-dependent parameters by updating **A** and **B** at each time step. In addition, this formulation also facilitates scalability for larger thermal networks by expanding **A, B** and **T** to include additional nodes [44].

3. Validation

To validate the proposed analytical thermal network model, a comparative analysis was conducted against CFD and experimental results from Kong *et al.*'s work [76]. It should be noted that, this study was chosen to validate our physical model as the authors fully disclose the properties and characteristics of the cell and PCM, along with the experimental conditions related to the battery's charge and discharge cycles. The experimental test [76] consists of wrapping 5 mm layer of PCM around a 21700 cylindrical cell type, then inserting it inside a thermostat incubator to maintain a fixed temperature of 30 °C with an incertitude range of ±1 °C. The test involves a fully charged battery to discharge with a constant current corresponding to a discharge rate of 3C, followed by cell charging with a charge rate of 0.5C and allowing for a 10-min idle period. Two consecutive repetitions of this procedure took place. K-type thermocouple with a diameter of 0.5 mm was fixed on the cell middle height. In the physical model the heat transfer coefficient between the PCM outer layer and surrounding air was set to 4 $W/m^2.K$ to match the natural convection inside the incubator.

As illustrated in Fig. 3 (a), the obtained battery surface temperature with the proposed model aligns with the experimental and CFD data; the model captures the transient temperature evolution during battery operation. The mean absolute error (MAE) and root mean square error (RMSE) between the proposed model and the experimental data are 0.167 °C and 0.269 °C, respectively. The difference obtained is below the typical accuracy range of K-type thermocouples of 0.5 °C. Furthermore, these quantitative metric values confirm the model's robustness in predicting thermal behaviour under dynamic conditions for real-world applications.

$$MAE=\frac{1}{N}\sum_{i=1}^{N}\left|T_{s_i}-T_{\exp_i}\right| \tag{19}$$

$$RMSE=\sqrt{\frac{1}{N}\sum_{i=1}^{N}\left(T_{s_i}-T_{\exp_i}\right)^2} \tag{20}$$

The model was also compared to the experimental data from Ref. [77], where the surface temperature of the 18650 LIB type was measured using a K-type thermocouple (accuracy of ±0.2 % + 1 °C) during continuous discharge at a 3C current. The battery was maintained at a controlled temperature of 22 °C. Fig. 3 (b) indicates that the relative error of the lumped model in comparison to the experimental data is below 4 %, hence confirming the model's validity.

4. Results and discussion

This paragraph comprises the parametric study regarding the impact of the thermo-physical properties of the bPCM, as well as the cell characteristics, on the thermal behaviour of the battery during three successive charge–discharge cycles. The discharge is carried out at a 3C-rate current, while charging is performed at a 1C-rate, with a 10 min rest period between the charging and discharging phases to allow the battery to reach thermal and chemical equilibrium. This procedure allows us to verify the capacity of the BTMS to control cell temperature under typical conditions.

Table 3 shows the cell and bPCM properties and the ranges of the parameters studied. The study will cover the effects of several parameters related to battery and bPCM characteristics, ambient conditions, and the driving cycle current profile. This section is structured to first present the influence of bPCM-related characteristics in section 5.1, followed by an examination of the effects of key cell parameters in section 5.2, and finally, sections 5.3 and 5.4 address the influence of ambient conditions and realistic discharge conditions, respectively.

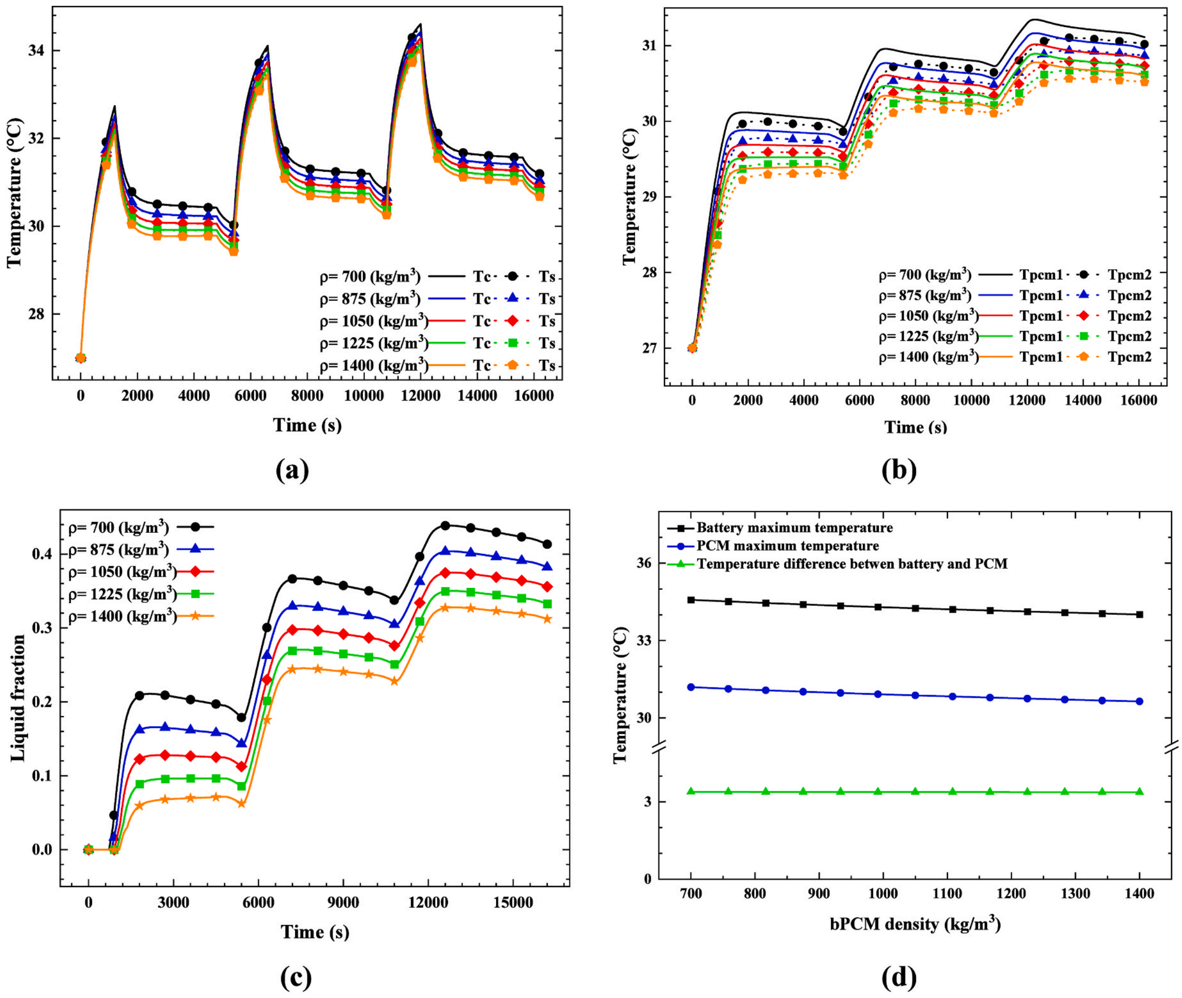

Fig. 9. Effect of bPCM density on (a) Battery core and surface temperature, (b) Temperature distribution in bPCM zones 1 and 2, (c) Global liquid fraction, (d) Maximum battery and bPCM temperatures.

4.1. *Parametric study of bPCM related characteristics*

This subsection analyses the impact of various bPCM properties on the thermal behaviour of the Li-ion cell under three consecutive charge–discharge cycles. For each parameter, we report the temperature profiles at the cell core, cell surface, bPCM zones 1 and 2, the global liquid fraction of the bPCM, and the maximum temperatures reached.

4.1.1. *Effect of bPCM layer thickness*

The amount of bPCM surrounding the cylindrical cell is a key factor in the thermal management of batteries. To investigate its effect on thermal performance, the bPCM volume was adjusted by varying the bPCM thickness around the cell. The physical model used in this study only takes into account heat transfer by conduction within the bPCM. This approach is valid when natural convection is neglected, a condition that is satisfied in configurations where the aspect ratio (AR) of the bPCM exceeds 6 [58]. The thickness of the bPCM ranges from 1 mm to 12 mm, corresponding to AR values between 70.9 and 5.9, respectively. It is important to note that the case with the maximum thickness of 12 mm (AR = 5.9) falls slightly outside this conduction-only regime. Indeed, for small volumes and in confined configurations, fluid movements (liquid phase) induced by density variations can be restricted by the homogeneous distribution of cells within a battery pack, which prevents the establishment of significant convective structures. However, in order to rigorously confirm this hypothesis in the limit case (AR = 5.9), a CFD simulation could be considered. This would allow for the confirmation of the system's status relative to the critical threshold of thermal instability, thus validating the hypothesis of purely conductive heat transfer.

We also calculated the Biot number for both the cell and the bPCM across different layer thicknesses. Evaluating this dimensionless number helps us to verify whether the cell and the bPCM behave as thermally homogeneous bodies or whether significant internal temperature gradients must be considered within both the cell and the bPCM.

Fig. 4(a) and (b) show the temperature evolution at the centre and the shell of the cell, as well as in zones 1 and 2 of the bPCM, as defined in Fig. 1. Fig. 4(c) illustrates the evolution of the global liquid fraction of bPCM over time, and Fig. 4(d) illustrates the highest temperatures of the battery and bPCM in relation to the thickness of the PCM layer. According to the findings, the temperature gradient inside the cell remains negligible regardless of the quantities of bPCM used. The internal thermal gradient of the bPCM increases in proportion to the thickness of the layer. The thermal response of the battery and the bPCM varies consistently with the thickness employed. For the 1 mm case, there are large temperature fluctuations observed during the charging and discharging processes since the bPCM is fully melted at the beginning of the second discharge cycle, displaying the low longevity of the passive BTMS performance. When the thickness layer of the bPCM exceeds 3 mm, the fluctuations in magnitude of the cell and bPCM temperature are much restrained, especially during the discharge period where the battery is subjected to a high current load. Although the bPCM's ability to regulate temperature is demonstrated, as seen in Fig. 4(d). However, above 6 mm

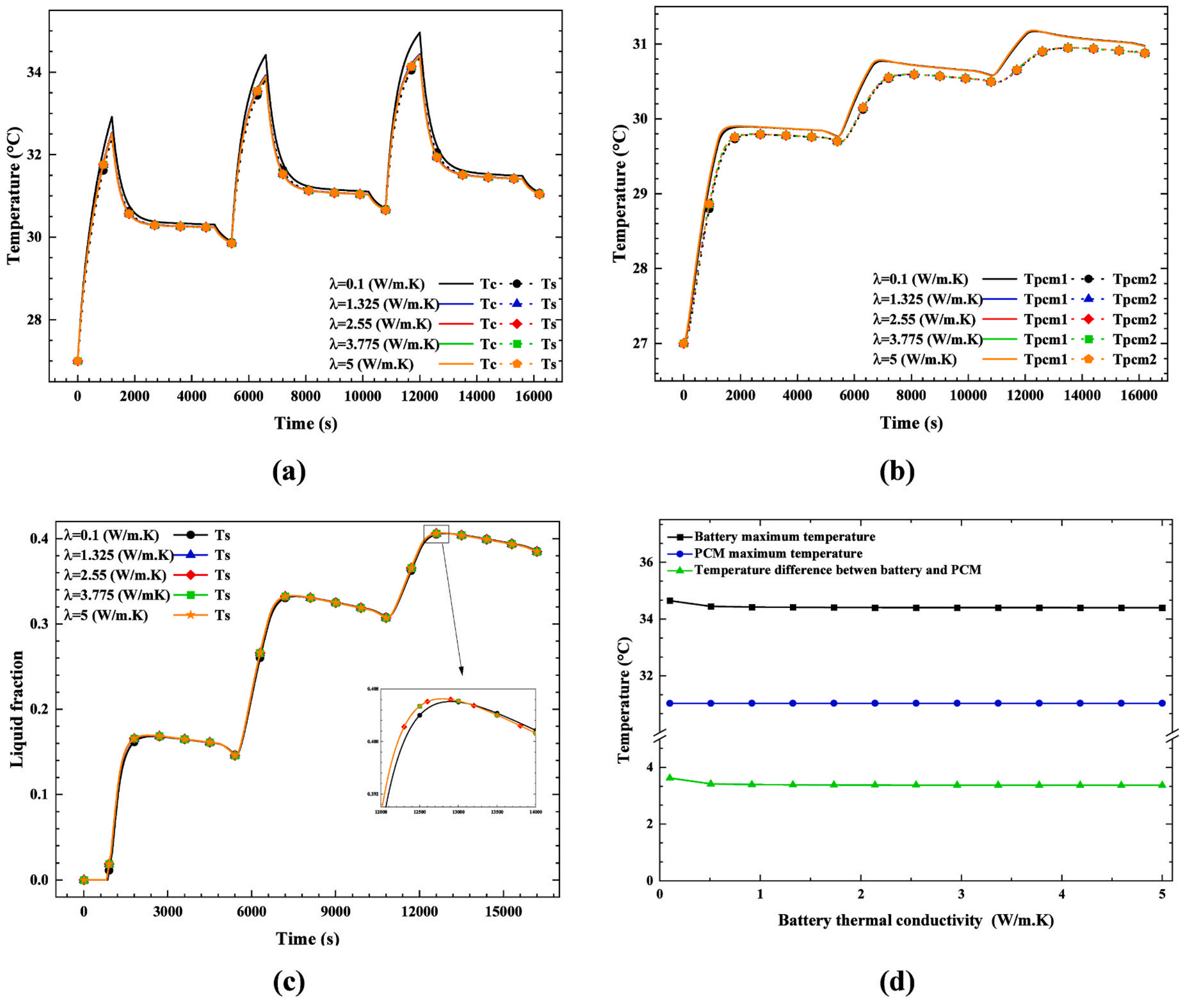

Fig. 10. Effect cell radial thermal conductivity on (a) Battery core and surface temperature, (b) Temperature distribution in bPCM zones 1 and 2, (c) Global liquid fraction, (d) Maximum battery and bPCM temperatures.

thickness, there is minor improvement remarked for the peak temperatures despite the addition of bPCM around the cell. Excessive addition of the materials can be disadvantageous due to increased weight, volume, and cost without any significant thermal benefit for the BTMS.

4.1.2. Effect of bPCM heat of fusion

Analogously, we explored the influence of latent heat, which reflects the ability of the bPCM to absorb heat without warming up during phase transition. A range of latent heat values were explored, spanning from **50** to 280 kJ/kg, and the remaining parameters were kept the same, following the default values outlined in Table 3. Fig. 5(a) and (b) show the temperature evolution within the cell and the bPCM, as indicated in Fig. 1. Through analysing these figures, it’s revealed that the effect of latent heat on the temperature evolution of the cell is relatively limited. The temperature fluctuations are damped progressively with the increase in latent heat values. The battery sustains a consistent internal temperature regardless of the latent heat value of the bPCM. Correspondingly, the temperature of the bPCM increases in a stepwise pattern, with these steps displaying a clear plateau shape at the higher latent heat. The liquid fraction profiles in Fig. 5(c) reveal that elevated latent heat values delay the melting of the bPCM, thereby extending the effective thermal regulation duration of the passive BTMS. This behaviour is particularly beneficial during repeated charge-discharge cycles, where the issue of thermal accumulation arises. The maximum temperatures decline proportionally with the increase of the latent heat for values lower than 200 kJ/kg as seen in Fig. 5(d). After this threshold, the maximum temperature remains almost constant, indicating no improvement in thermal regulation. In conclusion, while latent heat affects the thermal storage capacity of the bPCM, it does not lead to notable changes in the temperature distribution within the battery.

4.1.3. Effect of bPCM thermal conductivity

Assuming the same setup, the average thermal conductivity of the bPCM is examined in a spectrum from 0.1 to 5 W/m.K, while maintaining all other parameters at their default values following Table 3. In reality, the thermal conductivity of bPCM can be enhanced by introducing carbon- or metal-based materials [27,78]. Carbon fibre, expanded graphene, and graphene are known effective with small volume fraction, the thermal conductivity could be enhanced globally or along a specific direction [78]. The metal-based approach relies on nanoparticles, metal fibres and metal foam mostly. These additives enable reaching an apparent thermal conductivity exceeding 16.2 W m^{-1} K^{-1} [79], At a low conductivity value of 0.1 W/m.K, a slight change in cell temperature is noted when compared to the other conductivity values, as illustrated in Fig. 6(a). Furthermore, a notable thermal gradient develops within the bPCM, indicating poor heat distribution (see Fig. 6(b)). This gradient rapidly diminishes as the thermal conductivity increases, reflecting improved temperature uniformity throughout the bPCM. According to the liquid fraction profiles shown in Fig. 6(c), there is a minimal effect of increasing heat conductivity on the melting of the bPCM. The maximum temperatures recorded at the cell and within the bPCM remain nearly unchanged across the set of values

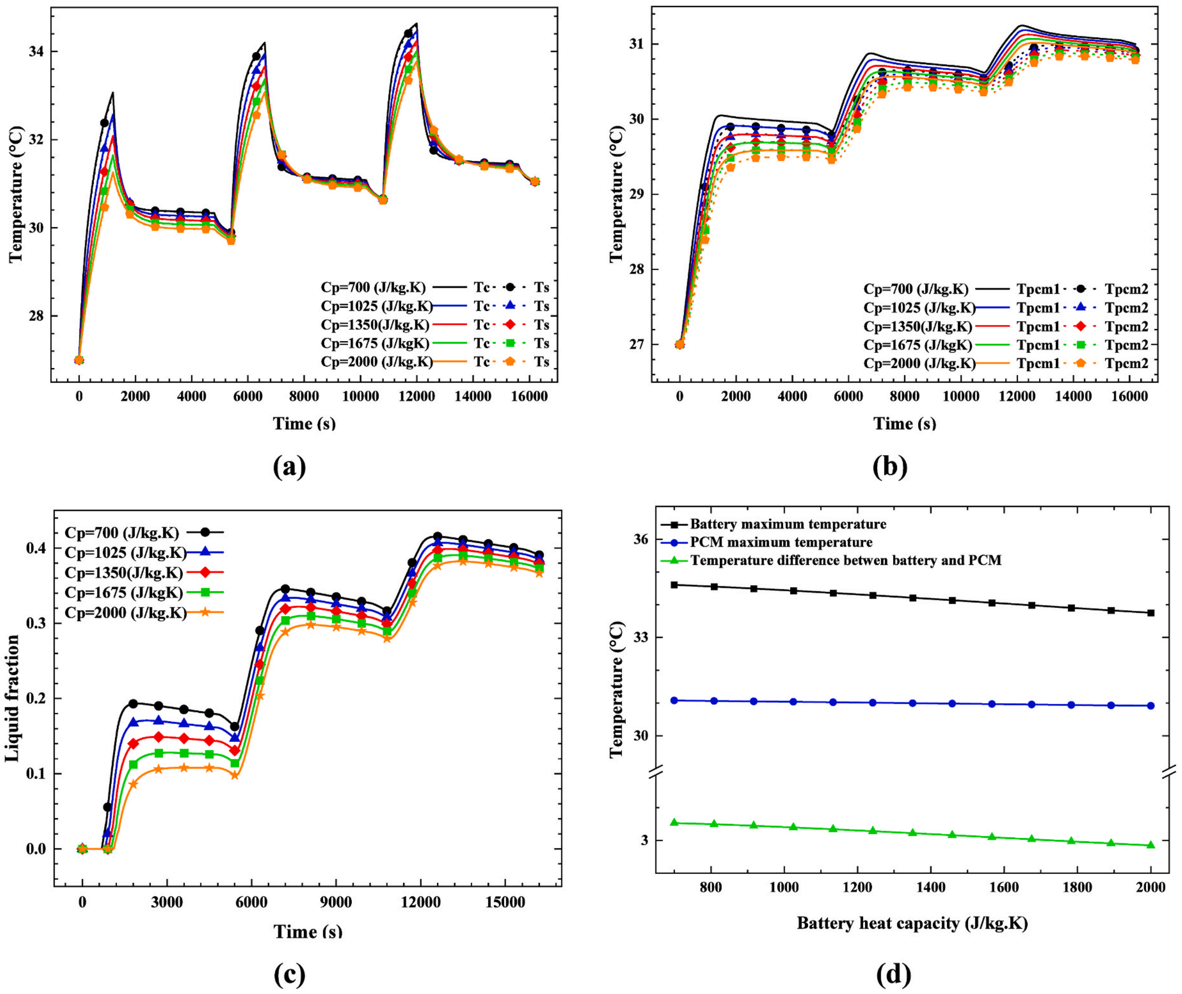

Fig. 11. Effect of cell heat capacity on (a) Battery core and surface temperature, (b) Temperature distribution in bPCM zones 1 and 2, (c) Global liquid fraction, (d) Maximum battery and bPCM temperatures.

Table 4
Cell format, volume, lateral surface area, and its ratio.

Battery format	Cell volume (mm^3)	Lateral surface area (LSA) (mm^2)	LSA to volume ratio (mm^{-1})
18650	16,540	3676	0.222
20700	21,991	4398	0.2
21700	24,240	4619	0.19
22700	26,614	4837	0.182
25700	34,361	5498	0.16
26650	34,516	5309	0.154
30700	49,480	6597	0.133
4695	157,875	13,729	0.087
4680	132,946	11,562	0.087

studied, as illustrated in Fig. 6(d). These findings suggest that, in this particular configuration, increasing the thermal conductivity of the bPCM has a limited effect on peak temperatures, although it significantly improves internal heat distribution within the bPCM.

4.1.4. Effect of cell-bPCM interfacial heat transfer coefficient

The interfacial heat transfer coefficient characterises the rate of thermal energy transfer between the battery cell surface and the surrounding bPCM layer, influenced by surface contact quality, bPCM thermal properties, and the geometry of the enclosure. As illustrated in Fig. 7(a), increasing this coefficient from 5 W/m^2.K to 100 W/m^2.K substantially reduces the battery temperature peaks and accelerates battery surface cooling, indicating effective heat extraction. The temperature profiles in bPCM zones (Fig. 7(b)) reveal that higher convective heat transfer values lead to faster bPCM melting, with the liquid fraction profiles in Fig. 7(c) confirming accelerated phase change rates. Remarkably, the maximum battery temperature declines hyperbolically with increasing the convective transfer coefficient, while the bPCM temperature remains constant, as depicted in Fig. 7(d). The effect of the interfacial heat transfer on cell and BTMS functioning diminishes above 50 W/m^2.K.

4.1.5. Effect of bPCM melting temperature

We evaluated the influence of the phase change temperature of the bPCM on the thermal performance of the cell, varying this temperature within a range from 27.5 °C to 37.5 °C. All other parameters were kept constant, in accordance with the default values listed in Table 3. The results indicate that the melting temperature plays a critical role in the cell temperature evolution, where the temperature curve increases as a function of melting points while maintaining the same pattern. Conversely, the internal temperature gradient of the cell and bPCM remains stable (see Fig. 8(a) and (b)). The liquid fraction profiles in Fig. 8 (c) indicate that a lower melting point of the bPCMs offers superior initial temperature control, they also achieve complete melting sooner, which may diminish thermal regulation effectiveness over prolonged use. In Fig. 8(d), lowering the melting temperature leads to a noticeable reduction in the maximum temperatures observed at both the cell and the bPCM levels. This behaviour can be attributed to the fact that a

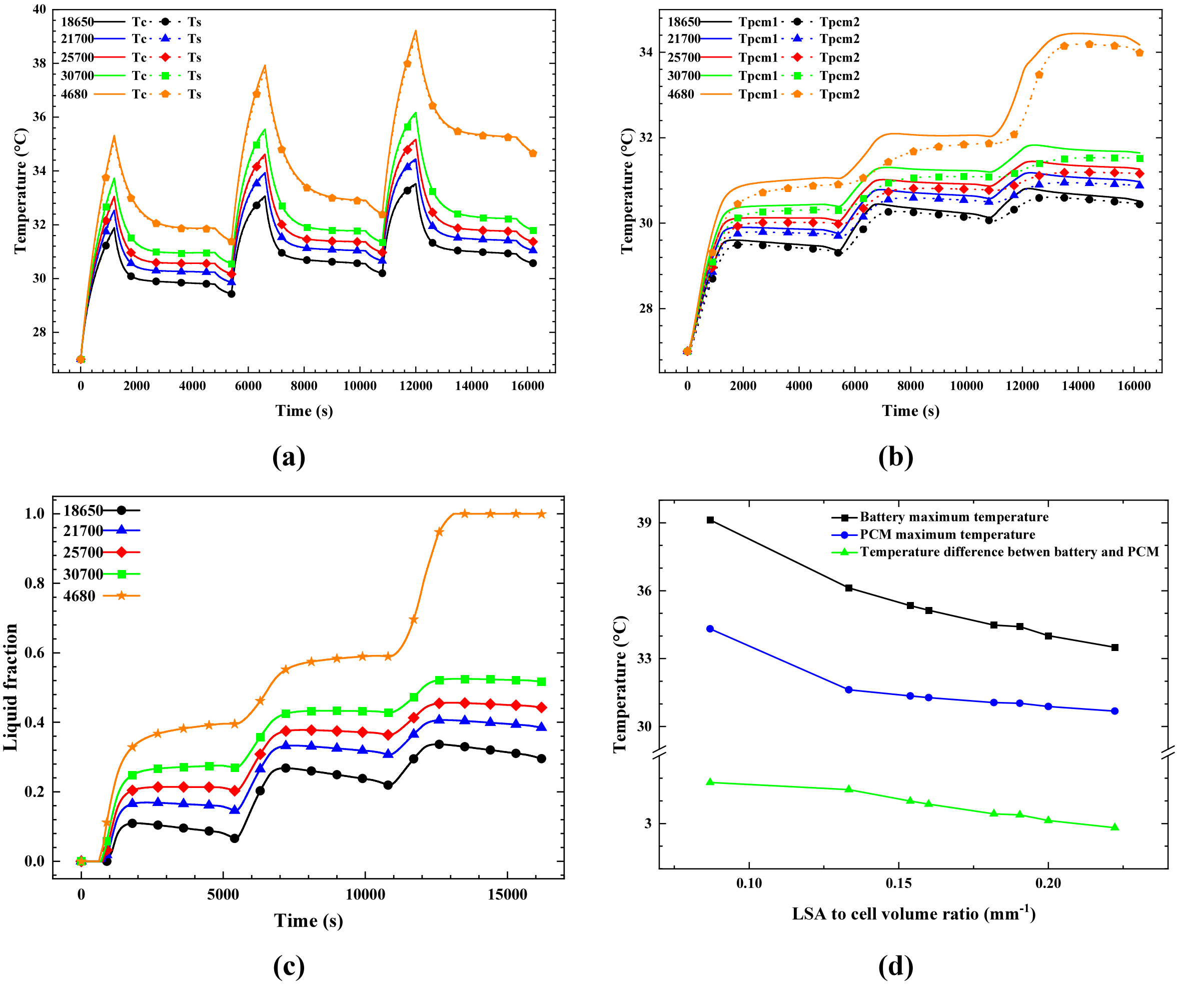

Fig. 12. Effect of interfacial heat transfer coefficient between bPCM and cell on (a) Battery core and surface temperature, (b) Temperature distribution in bPCM zones 1 and 2, (c) Global liquid fraction, (d) Maximum battery and bPCM temperatures.

bPCM with a lower melting temperature begins absorbing heat earlier, thereby limiting the cell temperature rise more effectively. These findings highlight the importance of selecting an appropriate melting temperature for efficient thermal management. In the configuration studied, reducing the melting temperature significantly improves thermal regulation.

4.1.6. *Effect of bPCM density*

Another key parameter we examined in this study is the impact of the average density of the bPCM on the thermal performance of the battery. As shown in Fig. 9(a) and (b), varying the average density of the bPCM between **700** and 1400 kg/m^3 does not significantly affect the thermal gradients within the cell and the bPCM. The liquid fraction profiles in Fig. 9(c) reveal that denser PCMs undergo slow gradual phase transitions, extending the effective thermal regulation duration across multiple charge-discharge cycles. In fact, the maximum temperatures measured both at the cell and bPCM levels remain unchanged, regardless of the different bPCM density values (see Fig. 9(d)). This suggests that, for this specific configuration, the bPCM density does not have a notable impact on the thermal management of the battery. However, a bPCM with a higher density allows for maximum thermal storage capacity within a confined volume. The result helps to optimise the available space, which becomes a key factor in enhancing the energy efficiency and overall performance of the battery.

4.2. *Parametric study of cell-related parameters*

This subsection evaluates the influence of variations in battery thermo-physical and geometric parameters on the thermal response of the battery-bPCM system. The conditions and parameter values are maintained as in Section 5.1, where the bPCM parameters are listed in Table 3. The assessment relies on temperature evolution, liquid fraction behaviour, and peak temperatures as key indicators for BTMS performance.

4.2.1. *Effect of cell radial conductivity*

We studied the impact of the thermal conductivity of the Li-ion cell on its overall thermal performance. This physical property is crucial, as it determines the cell's ability to effectively dissipate the heat generated during its operation while influencing the internal thermal gradient. According to the literature, the thermal conductivity of LIB exhibits anisotropic behaviour [55]. In other words, heat does not propagate uniformly in all directions. Two main conduction axes are typically considered: the axial direction (along the axis of the cell) and the radial direction (perpendicular to this axis). These two directions have different thermal conductivity values, which **are** directly related to the internal structure of the cell, especially the jelly roll arrangement of the electrode layers and separators [80].

Thermal conductivity values in each direction vary depending on the type of cell (cylindrical, prismatic, pouch) and the materials used. However, this thermal anisotropy significantly affects the temperature distribution inside the cell, which in turn influences the efficiency of

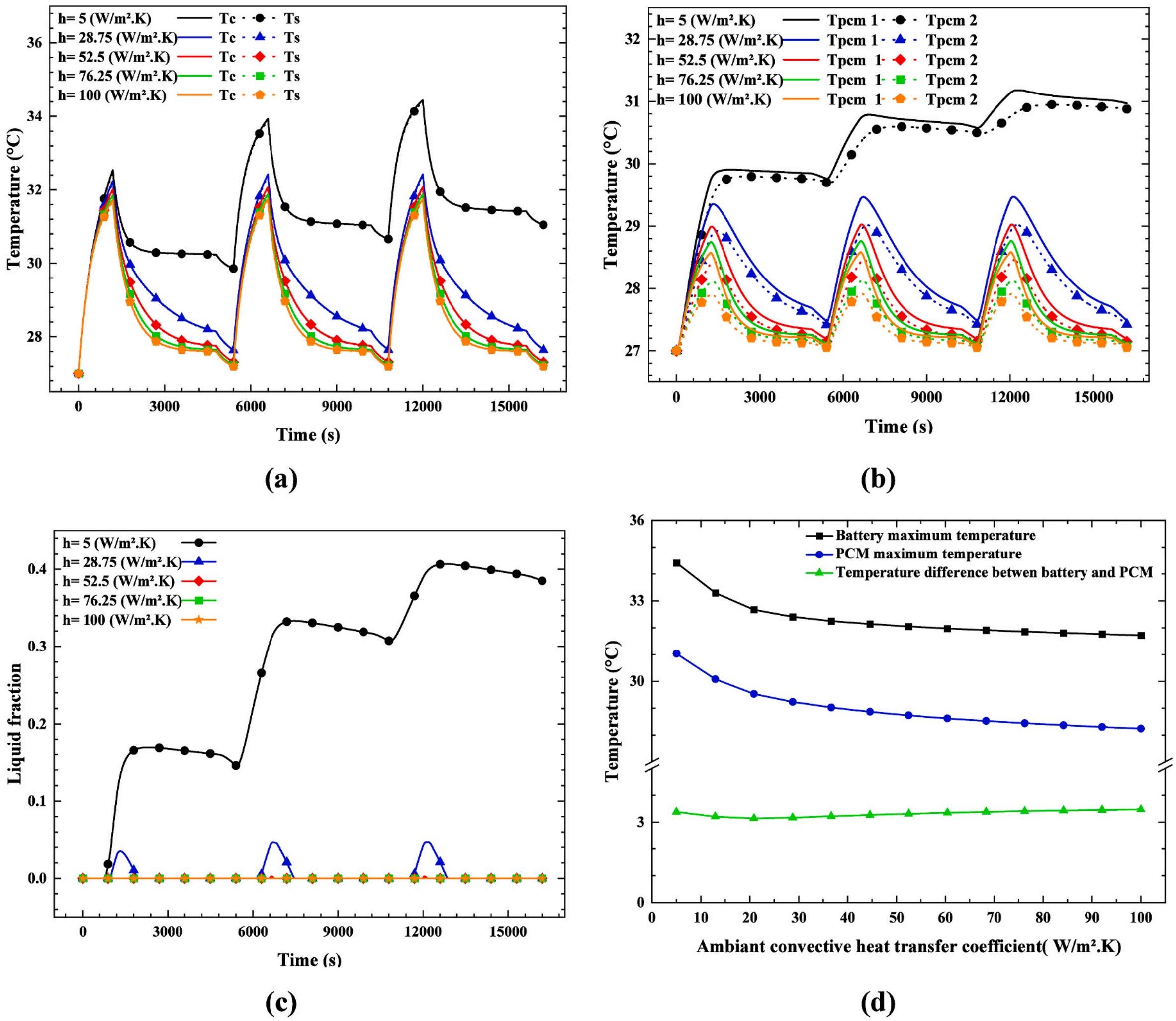

Fig. 13. Effect of heat transfer coefficient on (a) Battery core and surface temperature, (b) Temperature distribution in bPCM zones 1 and 2, (c) Global liquid fraction, (d) Maximum battery and bPCM temperatures.

thermal management solutions, such as bPCM. The performance of these materials is highly dependent on their ability to absorb and redistribute heat generated by the cell. In our case, where the studied cell is cylindrical, the literature typically reports a radial thermal conductivity ranging from **0.1** to 5 W/m.K**,** while the axial conductivity can vary between 6 and 36 W/m.K [53]. This significant difference confirms the highly anisotropic nature of thermal conduction in this type of cell. In this study, as mentioned at the beginning of the article, we chose to consider only the radial thermal conduction. This choice is based on the assumption that radial conduction plays a predominant role in cylindrical Li-ion cells. Consequently, we neglected axial conduction, although it can also influence thermal dissipation, particularly in prismatic or pouch cells.

Fig. 10(a) and (b) illustrate the effect of radial thermal conductivity on the temperature evolution within the cell. When the thermal conductivity value is set to 0.1 W/m.K, a temperature gradient within the cell emerges. The slow heat diffusion allows the inner cell temperature to increase compared to the shell area, this gradient becomes less steep as the value of the cell's thermal conductivity rises. The bPCM temperature evolution is slightly influenced by the cell heat conductivity, as seen in Fig. 10(b). The cell thermal conductivity does not affect the temperature pattern or the internal gradient. The liquid fraction in Fig. 10(c) is consistent across the examined thermal conductivity values, with insignificant fluctuations noted for the case with the lowest thermal conductivity. Additionally, the peak temperatures in both the cell and the bPCM stay the same, with the exception **of** the lowest cell thermal conductivity, as shown in Fig. 10(d). These results highlight the role of the thermal conductivity in dissipating generated heat within the cell; low radial conductive heat can create a high thermal gradient inside the cell. Consequently, the low radial conductive heat is affecting the cell's electrochemical behaviour.

4.2.2. *Effects of cell heat capacity*

This section covers the impact of the cell's specific heat capacity on the overall thermal performance of the passive BTMS. This thermophysical characteristic shows how much heat is needed to raise the temperature of 1 kg of cell by 1 K. With a larger heat capacity, the cell is able to buffer instant shifts in temperature, especially during high C-rate charging and discharging, thereby improving thermal stability and lowering the chances of overheating. The specific heat capacity of LIB in the literature is generally identified using inverse techniques [53,81,82]**.** This method involves adjusting the parameters of a thermal model based on experimental data obtained under controlled conditions, resulting in a representative value for the cell's thermal behaviour. The specific heat capacity depends on the chemistry, geometry, and architecture of the cell, typical values for cylindrical shape**s** are reported in the range from **700** to 2000 J/kg.K [53].

Fig. 11(a) and (b), and 11(c) illustrate the impact of the cell's specific heat capacity on the overall thermal performance of the LIB. More specifically, these figures show the temperature's evolution within the

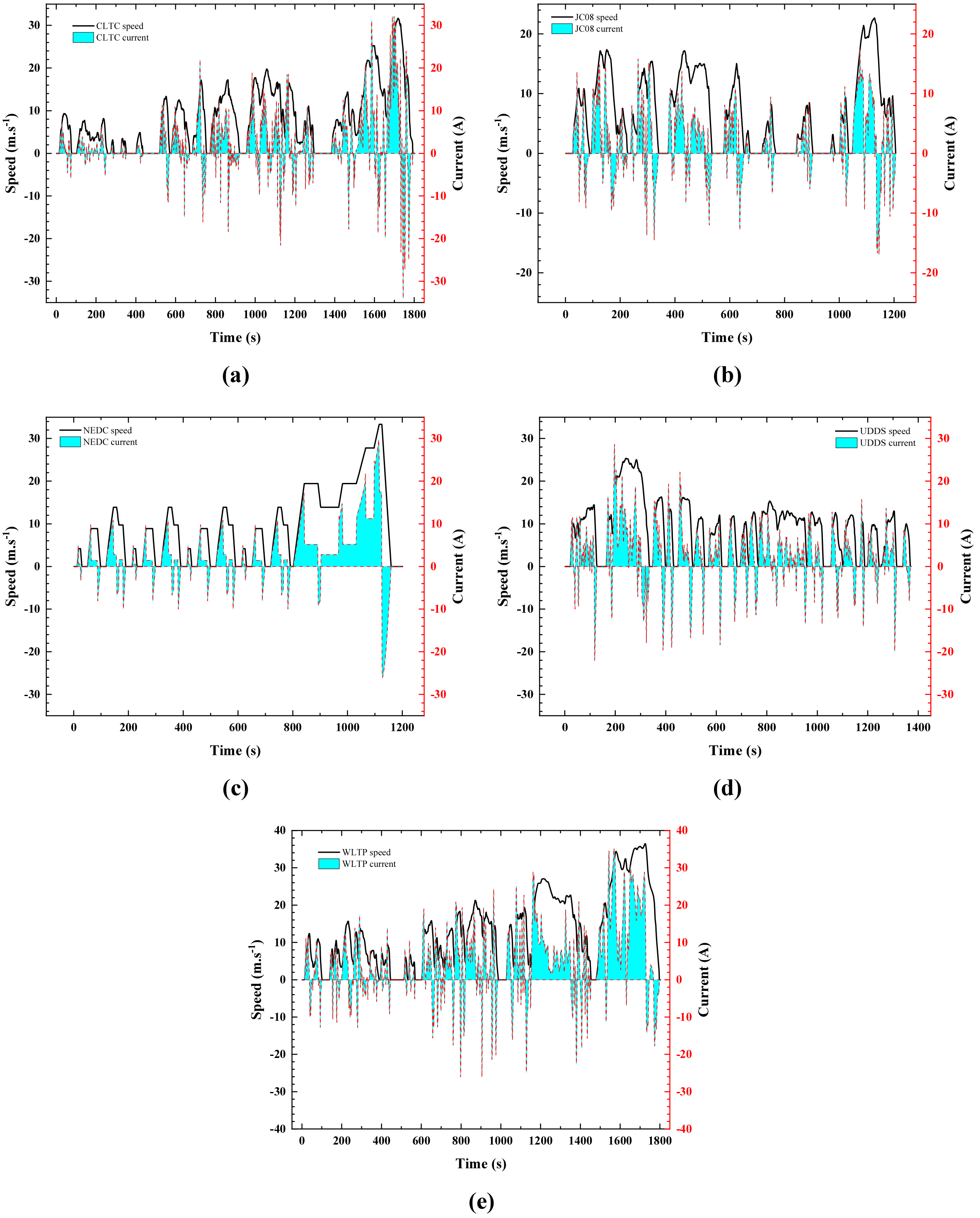

Fig. 14. Driving cycle speed profile and its corresponding current, (a) CLTC, (b) JC08, (c) NEDC, (d) UDDS, (e) WLTP.

cell, within the bPCM, and the time-dependent variation of the bPCM's liquid fraction for different values of the cell's heat capacity. The fluctuations in cell temperature over time are dampened with the increase of cell heat capacity; the peak temperatures at the end of the discharge process of each case are dissimilar, while equal temperatures are attained during the cell charging period, as seen in Fig. 11(a). In fact, this remark can be explained by the low specific heat that enables the cell to store a small amount of heat before its temperature rises. The unabsorbed heat by the cell is propagated to the surrounding bPCM to increase its temperature, which aligns with Fig. 11(b) trend. The lower the cell heat capacity, the higher the amount of heat absorbed by the melting process, which in turn impacts the evolution of the liquid fraction. A careful look at Fig. 11(a) reveals that the difference between the peak temperatures of the different cases was reduced between each successive charge-discharge cycle. In reality, in the first cycle, the cell with a heat capacity of 2000 kJ/kg.K was able to store a high amount of heat during discharge without massively increasing its temperature. Then during the charging period, it releases the stored heat to the surrounding bPCM, explaining the high jump in liquid fraction in Fig. 11(c). At the beginning of the second cycle, the cell was already warm, so its

Table 5
Reference value for driving cycle conversion.

Symbols	Meaning	Unit	Value
ρ	Air density	$(kg.m^{-3})$	1.204
S	Frontal area of the car	(m^2)	2
c_x	Drag coefficient		0.3
c_R	Rolling coefficient		0.01
mt	Total mass of the car	(kg)	1500
υ	Speed of the vehicle	$(m.s^{-1})$	DC profile
g	Gravitational acceleration	$(m.s^{-2})$	9.81
a	Vehicle acceleration	$(m.s^{-2})$	DC profile
η_{motor}	Motor efficiency	(%)	90
η_{cont}	Controller efficiency	(%)	90
η_{conv}	Converter efficiency	(%)	95
V_{pack}	Battery pack voltage	(V)	365

Table 6
Cell electrical capacity balance for different DC.

Driving cycle	CLTC	JC08	NEDC	UDDS	WLTP
Electrical capacity drawn from the cell (Ah)	1.475	0.805	1.119	1.233	2.784
Electrical capacity injected to the cell (Ah)	−0.562	−0.354	−0.348	−0.538	−0.766
Total cell electrical (Ah)	0.913	0.45	0.771	0.695	2.018

capacity to store heat was limited, which reflects the low difference between the cases in terms of peak temperature. This tendency is repeated in the third cycle as well, damping this difference even further. As illustrated in Fig. 11(d), the maximum temperatures of both the cell and the bPCM are inversely proportional to the cell heat capacity with a slight curve slope. Cells with higher heat capacity reduce the reliance on active BTMS to regulate temperature. Especially in the electric vehicle context where a large number of cylindrical cells are assembled to form battery packs.

4.2.3. *Effects of battery size*

This section covers the impact of cylindrical cell formats available commercially, spanning from the standard 18650 cell to the newest formats like 4680 [57,83–85]. The smallest 18650 format has a diameter of 18 mm and a height of 65 mm, whereas the biggest 4680 format is characterised by a diameter of 46 mm and a height of 80 mm [86]. As cell technology advances, the latest generation of cells represents a significant advancement in battery technology, particularly for EVs due to their high power and energy density. To compare the influence of formats objectively, the core cell diameter to overall cell diameter ratio is set to 0.92. Additionally, the volumetric heat generation is assumed identical for the studied cell formats, and the cell density is set at 2630 kg/m^3. Under these conditions, only the battery format influences heat propagation within the BTMS; the cell formats studied are tabulated in Table 4.

Fig. 12(a) depicts the temperature evolution over time for the 18650, 21700, 25700, 30700, and 4860 cell types. The temperature fluctuations during the charge and discharge process are enlarging as the cell format increases. This trend is explained by the supplementary heat related to the cell's increased volume and lateral surface area (LSA) to volume ratio. In fact, this ratio is inversely proportional to the radius of the cell, regardless of its height. In comparison to their heat-generating volume, cells with a narrow radius have a proportionately larger surface area for heat dispersion, which results in more effective cooling. The temperature profiles in bPCM zones (Fig. 12(b)) and liquid fraction evolution (Fig. 12(c)) confirm that larger format cells with larger diameters drive more rapid bPCM melting, exhausting the thermal regulation capacity of passive BTMS earlier in the cycling process. Fig. 12(d) illustrates the evolution of the maximum temperatures observed inside the lithium-ion cell as well as in the bPCM, as a function of the cell's LSA to volume ratio (2/r). The maximum temperature of the cell is inversely proportional to cell radius, suggesting a high effect of the convection mode in regulating the temperature of the cell. A similar pattern is observed in the bPCM maximum temperature, with a lower figure slope related to the latent heat of the phase transition. Overall, regardless of the cell volume, the LSA to volume ratio is a key indicator for characterising the thermal behaviours of the cell.

4.3. *Effect of ambient convective heat transfer coefficient*

The convective heat transfer coefficient between the bPCM outer surface and its environment is covered in this section. It reflects the ambient conditions under which the LIB operates, including the fluid nature, the flow velocity, and the geometry of the battery itself. These factors can significantly change the convective coefficient, affecting passive BTMS thermal performance. In this analysis, the coefficient is varied within a range from 5 to 100 $W/m^2.K$, while the ambient temperature was maintained at 27 °C to simulate typical summer conditions in temperate climates.

As depicted in Fig. 13(a), the temperature evolution of the cell under different values of ambient conditions reveals a massive difference in the thermal response. The peak temperature at the end of the discharge process decreases as the convective coefficients increase. Furthermore, during the charging period, the battery temperature is cooled at different rates, which are affected by the ambient convective coefficient. Under a value of 5 $W/m^2.K$, the battery maintains a stable temperature during charging, and it's heated during discharge. This pattern is also observed in the bPCM temperature and the corresponding liquid fraction, suggesting poor heat dissipation to the ambient, which affects the regulation role of the passive BTMS. For higher values of the convective heat transfer coefficient, the bPCM temperature profile exhibits a periodic pattern, where the temperature rises and reaches its maximum at the end of the discharge, then it cools during the charging period (see Fig. 13(b)). This cyclic behaviour is explained by the liquid fraction, where only a small amount of bPCM is melted at the end of the discharge process, as seen in Fig. 13(c), thereby restoring its thermal regulation capacity. Furthermore, an increase in the convective coefficient value leads to an increase in the thermal gradient inside the bPCM. In fact, the efficient heat transfer with the ambient maintains a lower temperature in the bPCM exterior zone, explaining the growing thermal gradient with a small dephasing effect. Furthermore, Fig. 13(d) demonstrates that maximum temperatures in both the cell and the bPCM decrease with increasing convective coefficient, with the most significant improvements observed in the range of 5–40 $W/m^2.K$.

4.4. *Effect of realistic driving cycle*

The driving cycle (DC) reflects the real-world operation of an electric vehicle on a route, including acceleration, braking, average speeds, and frequent stops. Depending on the intensity and frequency of the electric motor's operation, the battery generates varying amounts of heat, which alters its internal temperature and, consequently, affects its performance, lifespan, and safety. Current DCs are generally standardised and designed to simulate realistic driving conditions that are specific to different regions of the world. In this study, a representative set of driving cycles from the United States (UDDS), China (CLTC), Europe (NEDC, WLTP), and Japan (JC08) was selected (see Fig. 14) [87,88]. These DCs exhibit differences in speed profiles, acceleration and deceleration rates, and overall duration. This variation directly influences the heat generation profile of the cells. The Worldwide Harmonized Light Vehicles Test Cycle (WLTC), for instance, stands out due to its high peak and average speeds, reflecting a dynamic and aggressive driving style that results in significant thermal stress. In contrast, the Japanese JC08 cycle is characterised by lower averages and maximum speeds, which represent dense urban driving with frequent stops and starts, leading to more moderate thermal loads [89]. For the thermal assessment, the cell is initially charged, then it is discharged following the current profile

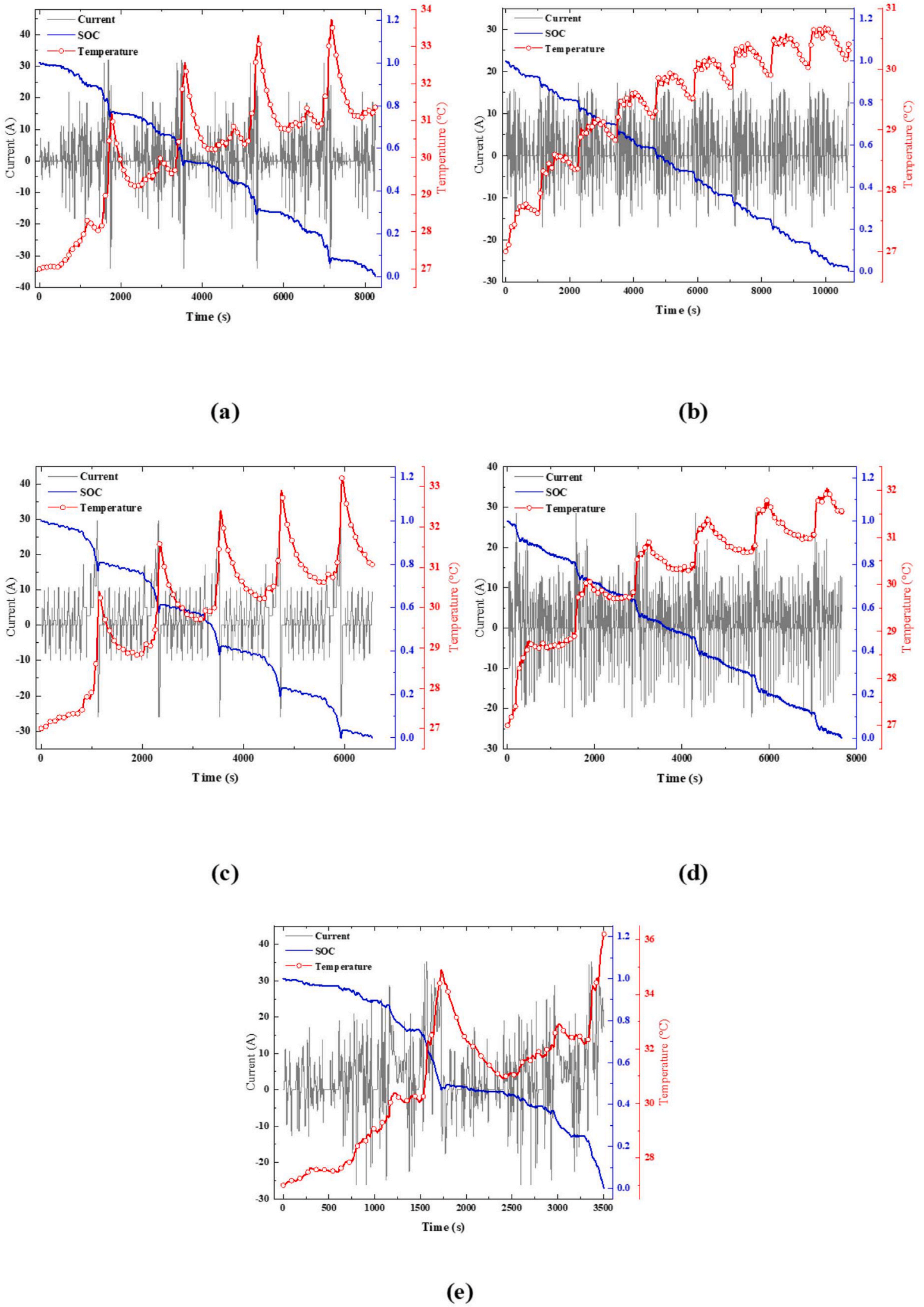

Fig. 15. Cell temperature evolution under realistic discharge current, and cell state of, (a) CLTC, (b) JC08, (c) NEDC, (d) UDDS, (e) WLTP.

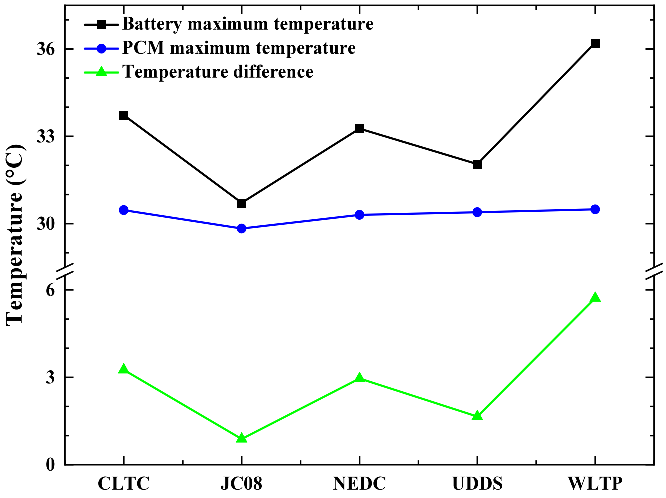

Fig. 16. Maximum PCM and battery temperature for different driving cycle profiles.

from each DC. This methodology enables the evaluation of the thermal accumulation effects during the extended operation period.

To quantify the thermal impact of each DC, a conversion from speed-time to current-time series is necessary. The conversion is achieved using a force balance approach that integrates the effects of rolling resistance, aerodynamic drag, inertial acceleration, and gravitational forces acting on the vehicle. This approach considers regenerative braking during deceleration and efficiency losses in the different components. The instantaneous battery current is expressed as [90]:

$$I = \frac{\frac{1}{2}.\rho.S.c_x.v(t)^3 + c_R.m_t.g.v(t) + m_t.a(t).v}{\eta_{motor}.\eta_{cont}.\eta_{conv}.V_{pack}} \tag{21}$$

Where, $v(t)$ and $a(t)$ are the time variation of vehicle velocity and acceleration extracted from the corresponding DC profile. The relevant parameters and their values of a standard light-duty vehicle are listed in Table 5 [91]. The nominal voltage and capacity of the cylindrical cell are 3.6 V and 4 Ah, as shown in Table 3. A battery pack with a 100s5p configuration is utilised in this study. The purpose of operating a small number of parallel chains is to replicate severe load conditions on the cells.

Converting the DC into the current cycle profile reveals some distinguished properties. The cell current can be positive, indicating the current drawn from the cell, or negative, indicating the injected current resulting from regenerative braking, a feature unique to EVs. Table 6 encompasses the cell electrical capacity balance for each DC to quantify the impact of regenerative braking. In JC08 and UDDS, the cell restates 44 % of its electrical capacity during deceleration, allowing the cell to power a long trajectory. Meanwhile, this percentage drops to 27.5 % in WLTP due to the low deceleration rate. Cell heat generation primarily correlates with the cell current; therefore, varying current profile behaviour will significantly differentiate the thermal response.

Fig. 15 shows the current demand, state of charge (SOC), and temperature evolution of the cell under CLTC, JC08, NEDC, UDDS, and **WLTP** DC profiles. Each one enables the cell to discharge at different current values, affecting the time required to fully discharge it. Overall, the SOC curve decreases over time, with fluctuations reflecting the charge and discharge of the cell. For CLTC, NEDC, UDDS, and WLTP, the SOC curve decreases almost linearly with time. A steep decrease was observed at the end of each cycle, designating the high current drawn from the cell at these periods. The steep decrease observed in SOC differs from one DC profile to another. Conversely, the JC08 profile lacks this steep decrease pattern (Fig. 15(b)), suggesting that the cell draws a small amount of current. This specific difference in the current profile across the DCs investigated leads to diverse thermal cell responses. Under the CLTC and NEDC profiles, cell temperatures increase with cyclical behaviours, following the current pattern. In the first cycle, the temperature curve increases and reaches its peak value by the end of it. The cell's temperature first drops at the start of the second cycle and then rises at its conclusion. Until the cell discharges, this tendency repeats consecutively. Under both the JC08 and UDDS current loads, the temperature exhibits similar cycling behaviour. Each cycle features distinct periods of warming and cooling. Nevertheless, the temperature of the cell maintains its tendency to increase over time, reaching 30.71 °C and 32.04 °C, respectively. Under WLTP current load, the cell temperature increases with a distinguished two-cycle pattern. Where the temperature increases sharply, especially near the end of the first cycle, afterwards the curve slope decreases at the beginning of the second cycle, before the temperature starts to increase at the end of the second cycle to reach its peak value of 36.2 °C. Under high load DCs, the bPCM was able to regulate and maintain the cell in the optimal operational temperature range for LIB [92].

Fig. 16 illustrates a comparative analysis of the maximum temperatures reached in both the cell and bPCM under the investigated DCs. The analysis reveals that the maximum temperatures reached vary significantly depending on the applied DC profile. Specifically, the WLTP profile stands out with higher battery maximum temperatures compared to the other realistic profiles. The peak temperatures of JC08 and UDDS are the lowest, measuring 30.71 °C and 32.04 °C, respectively. This difference can be attributed to the demanding dynamic characteristics of the DCS, such as higher acceleration frequencies, greater average speeds, and more intense current demand. These factors place additional stress on the battery, leading to an immense heat generation rate in a short period.

4.5. Design guidelines

This section summarises the main conclusions drawn from the parametric study described in the previous sections, so as to define a set of recommendations regarding the design of compact passive multi-cell BTMS systems, particularly under heavy loads.

The results of our study indicate that bPCM thickness has a diminishing return beyond 6 mm on the maximum cell temperature. More specifically, for thinner cells such as 18650 and 21700, a 4 mm layer of bPCM is sufficient to maintain an acceptable cell temperature, while large format cells (4680) require a thicker layer of more than 6 mm. In battery pack configurations, partitioning bPCM between cells reduces total thermal loads while maintaining optimal average cell temperature conditions.

The thermophysical characteristics of bPCM also have a greater or lesser impact on the performance of passive BTMS depending on the external environment associated. The melting temperature of bPCM is an important parameter; it is recommended to choose a bPCM with a melting point 2–5 °C higher than the maximum ambient temperature in temperate climates (20–30 °C). For regions with hot climates, the use of a hybrid BTMS is strongly recommended, especially when the ambient temperature exceeds 35 °C. However, it is important to note that hybrid BTMS systems tend to be heavier and bulkier compared to passive systems, which presents challenges related to cost, maintenance, and management for battery applications.

The ability of bPCM to absorb excess heat is determined by its latent heat of fusion. Our findings indicate that a bPCM with a latent heat exceeding 150 kJ/kg should be chosen. For optimal performance of the passive BTMS proposed, thermal conductivity can be improved using several techniques. In the case of electric vehicles, improving the thermal conductivity via expanded graphite or carbon nanotubes is particularly effective for maintaining a uniform temperature within the battery pack. As the density of the bPCM has a minimal effect on the thermal performance of passive BTMS, low-density bPCMs are therefore recommended.

5. Conclusion

The comprehensive parametric analysis presented in this study provides valuable design insights for optimising bPCM-based BTMS. This study proposes and validates a two-state analytical thermal network model for cylindrical LIBs integrated with passive BTMS. The analysis considers the impact of both battery characteristics and the properties of bPCM on temperature evolution to assess the overall thermal performance. Among the parameters investigated, bPCM melting temperature, layer thickness, interfacial heat transfer coefficient and ambient conditions emerged as the most influential factors for reducing peak temperatures. A thickness of 6 mm was selected as the optimal solution, as it compromises thermal regulation, weight and volume. Employing a bPCM with a melting temperature below the maximum operating LIB threshold optimises heat absorption and extends the passive regulation period. While the thermal conductivity of the cell and the bPCM affects the internal temperature uniformity, its damping peak fluctuation effect is limited. The battery format is directly related to the heat generation rate and heat transfer process. The study elucidated the relationship between the cell radius and the peak temperature fluctuations through LSA to volume effects. The study also reveals the importance of ambient conditions, as they determine the heat dissipation of the BTMS and the regeneration of the thermal capacity of the bPCM. Under realistic DC loads the passive BTMS manages the excessive heat generated from the battery effectively, as the peak temperature during the discharge was maintained below 33 °C. These insights allow for a rapid and accurate evaluation of material characteristics, geometric configurations, and operating conditions, advancing the design of BTMS. Future work will explore scalability to battery packs with hybrid cooling strategies by extending the thermal network in three dimensions with additional nodes inside the cells to capture spatial temperature evolution. The parametric nature of the proposed model makes it a potential candidate for multi-objective optimisation by integrating weight, cost, and thermal performance metrics to identify optimal BTMS designs for specific scenarios.

CRediT authorship contribution statement

A. Afass: Writing – original draft, Software, Methodology, Investigation, Conceptualization. **S. Landini:** Writing – review & editing, Methodology, Formal analysis. **O. Elghaz:** Visualization, Validation, Formal analysis. **B. Lamrani:** Writing – review & editing, Visualization, Validation. **T. Kousksou:** Writing – review & editing, Supervision, Project administration.

Declaration of competing interest

The authors declare that they have no known competing financial interests or personal relationships that could have appeared to influence the work reported in this paper.

Acknowledgments

This project has received funding from the European Union's Horizon 2020 research and innovation programme under the Marie Skłodowska-Curie grant agreement No 945416.

Data availability

Data will be made available on request.

References

[1] N. Sharmili, R. Nagi, P. Wang, A review of research in the Li-ion battery production and reverse supply chains, J. Energy Storage 68 (2023) 107622, https://doi.org/10.1016/j.est.2023.107622.

[2] P. Juntree, S. Siriroj, J. Padchasri, P. Songsiririthigul, P. Kidkhunthod, Development of Li-ion batteries cathode materials by using nickel and cobalt mixed Li-borate base glass composite with V2O5 via melt quenching method, J. Alloys Compd. 1016 (2025) 178961, https://doi.org/10.1016/j.jallcom.2025.178961.

[3] B.E. Lebrouhi, S. Baghi, B. Lamrani, E. Schall, T. Kousksou, Critical materials for electrical energy storage: Li-ion batteries, J. Energy Storage 55 (2022) 105471, https://doi.org/10.1016/j.est.2022.105471.

[4] A. Komorowska, P. Olczak, Economic viability of Li-ion batteries based on the price arbitrage in the european day-ahead markets, Energy 290 (2024) 130009, https://doi.org/10.1016/j.energy.2023.130009.

[5] L. Singh, S. Kumar, R. Kumar, V. Srivastva, M. Bechelany, Y. Lee, Insights into solid solution-assisted polyanion cathodes: present status, environmental focus and advancement in phosphate and borate chemistry for Li- and Na-ion battery technologies, J. Alloys Compd. 1010 (2025) 177067, https://doi.org/10.1016/j.jallcom.2024.177067.

[6] R.G. Souza, A.M. Domingues, A. Spindlegger, C. Mair-Bauernfeind, F. Part, Review of the current knowledge and identified gaps in assessing the social and environmental impacts of mining processes in the Lithium Triangle, Sustain. Prod. Consum. 53 (2025) 40–63, https://doi.org/10.1016/j.spc.2024.11.031.

[7] B.E. Lebrouhi, Y. Khattari, B. Lamrani, M. Maaroufi, Y. Zeraouli, T. Kousksou, Key challenges for a large-scale development of battery electric vehicles: a comprehensive review, J. Energy Storage 44 (2021) 103273, https://doi.org/10.1016/j.est.2021.103273.

[8] H.H.M. Ali, Advances in high-performance concrete: a comprehensive review of materials, design, and applications, KHWARIZMIA 2023 (2023) 131–137, https://doi.org/10.70470/KHWARIZMIA/2023/013.

[9] W.A. Hammood, S.M. Asmara, M.M. Rosli, I.I. Ghdhban, E.U. Osiobe, Sensitivity analysis of electromechanical impedance signals for early detection of debonding in sandwich face layers: a case Study using SHM data, Mesopotamian Journal of Civil Engineering 2025 (2025) 1–19, https://doi.org/10.58496/MJCE/2025/001.

[10] X. Feng, M. Ouyang, X. Liu, L. Lu, Y. Xia, X. He, Thermal runaway mechanism of lithium ion battery for electric vehicles: a review, Energy Storage Mater. 10 (2018) 246–267, https://doi.org/10.1016/j.ensm.2017.05.013.

[11] S. Landini, J. Leworthy, T.S. O'Donovan, A review of phase change materials for the thermal management and isothermalisation of lithium-ion cells, J. Energy Storage 25 (2019) 100887, https://doi.org/10.1016/j.est.2019.100887.

[12] Z. Jia, K. Jin, W. Mei, P. Qin, Jinhua Sun, Q. Wang, Advances and perspectives in fire safety of lithium-ion battery energy storage systems, eTransportation 24 (2025) 100390, https://doi.org/10.1016/j.etran.2024.100390.

[13] M. Shahjalal, T. Shams, MdE. Islam, W. Alam, M. Modak, S Bin Hossain, et al., A review of thermal management for Li-ion batteries: prospects, challenges, and issues, J. Energy Storage 39 (2021) 102518, https://doi.org/10.1016/j.est.2021.102518.

[14] M.A. Bamdezh, G.R. Molaeimanesh, Impact of system structure on the performance of a hybrid thermal management system for a Li-ion battery module, J. Power Sources 457 (2020) 227993, https://doi.org/10.1016/j.jpowsour.2020.227993.

[15] M. Safdari, R. Ahmadi, S. Sadeghzadeh, Numerical and experimental investigation on electric vehicles battery thermal management under New European driving cycle, Appl. Energy 315 (2022) 119026, https://doi.org/10.1016/j.apenergy.2022.119026.

[16] E.S. Shrinet, A. Mukherjee, L. Kumar, A novel thermal management system design based on variable contact area to maintain uniform temperature in Li-ion battery module, J. Energy Storage 72 (2023) 108332, https://doi.org/10.1016/j.est.2023.108332.

[17] A. Moaveni, M. Siavashi, S. Mousavi, Passive and hybrid battery thermal management system by cooling flow control, employing nano-PCM, fins, and metal foam, Energy 288 (2024) 129809, https://doi.org/10.1016/j.energy.2023.129809.

[18] M. Shahmohammadi, S. Seddighi, A. Taklifi, Active and hybrid battery thermal management system using microchannels, and phase change materials for efficient energy storage, J. Power Sources 621 (2024) 235317, https://doi.org/10.1016/j.jpowsour.2024.235317.

[19] M.W. Nazar, N. Iqbal, M. Ali, H. Nazir, MZ Bin Amjad, Thermal management of Li-ion battery by using active and passive cooling method, J. Energy Storage 61 (2023) 106800, https://doi.org/10.1016/j.est.2023.106800.

[20] B. Al-Mistarehi, G. Ali, W. Robert, H. Hassan, The role of passive techniques in modern sustainable architecture, KHWARIZMIA (2024;2024) 105–117, https://doi.org/10.70470/KHWARIZMIA/2024/014.

[21] M. Nasiri, H. Hadim, Thermal management of Li-ion batteries using phase change materials: recent advances and future challenges, J. Energy Storage 111 (2025) 115440, https://doi.org/10.1016/j.est.2025.115440.

[22] E. Pilali, M. Soltani, M. Hatefi, S. Shafiei, M. Salimi, M. Amidpour, Passive thermal management systems with phase change material-based methods for lithium-ion batteries: a state-of-the-art review, J. Power Sources 632 (2025) 236345, https://doi.org/10.1016/j.jpowsour.2025.236345.

[23] H.B. Ghadim, A. Godin, A. Veillere, M. Duquesne, D. Haillot, Review of thermal management of electronics and phase change materials, Renew. Sustain. Energy Rev. 208 (2025) 115039, https://doi.org/10.1016/j.rser.2024.115039.

[24] J.F. Nicolalde, J. Martinez-Gómez, V.H. Guerrero, A. Chico-Proano, Experimental performance of avocado seed oil as a bio-based phase change material for refrigeration applications, Int. J. Refrig. 168 (2024) 632–647, https://doi.org/10.1016/j.ijrefrig.2024.10.006.

[25] A. Benhorma, A. Bensenouci, M. Teggar, K.A.R. Ismail, M. Arıcı, E. Mezaache, et al., Prospects and challenges of bio-based phase change materials: an up to date review, J. Energy Storage 90 (2024) 111713, https://doi.org/10.1016/j.est.2024.111713.

[26] S. Arun, R.J. Boche, P. Nambiar, P. Ekka, P. Panalkar, V. Kumar, et al., Numerical and experimental investigation on performance of thermal energy storage integrated micro-cold storage unit, Applied Sciences (Switzerland) 14 (2024), https://doi.org/10.3390/app14125166.

[27] A. Mitra, R. Kumar, D.K. Singh, Z. Said, Advances in the improvement of thermal-conductivity of phase change material-based lithium-ion battery thermal management systems: an updated review, J. Energy Storage 53 (2022) 105195, https://doi.org/10.1016/j.est.2022.105195.

[28] Sanker S. Babu, R. Baby, Phase change material based thermal management of lithium ion batteries: a review on thermal performance of various thermal conductivity enhancers, J. Energy Storage 50 (2022) 104606, https://doi.org/10.1016/j.est.2022.104606.

[29] R.K. Sinha, A. Kumar, A. Maurya, A. Kumar, Thermal management of counter terminal lithium-ion battery using Bio-based PCM, Therm. Sci. Eng. Prog. 54 (2024) 102854, https://doi.org/10.1016/j.tsep.2024.102854.

[30] S. Landini, W. Delgado-Diaz, R. Ravotti, R. Waser, A. Stamatiou, J. Worlitschek, et al., Effect of geometry and thermal mass of direct-metal-laser-sintered aluminium heat exchangers filled with phase change materials on Lithium-Ion cells' passive cooling, Appl. Therm. Eng. 195 (2021) 117151, https://doi.org/10.1016/j.applthermaleng.2021.117151.

[31] M.F. Junaid, Z ur Rehman, N. Ijaz, M. Čekon, J. Čurpek, A. Babeker Elhag, Biobased phase change materials from a perspective of recycling, resources conservation and green buildings, Energy Build. 270 (2022) 112280, https://doi.org/10.1016/j.enbuild.2022.112280.

[32] Y. Gao, Y. Zhao, X. Wang, M. Mohit, M. Xu, A.P. Sasmito, Review of supercooling suppression of phase change materials based on nanoparticles, Thermochim. Acta 745 (2025) 179936, https://doi.org/10.1016/j.tca.2025.179936.

[33] X. Li, W. Yang, L. Yin, S. Zhang, Y. Wu, Y. Mao, et al., Advancing lithium battery safety: introducing a composite phase change material with anti-leakage and fire-resistant properties, eTransportation 23 (2025) 100387, https://doi.org/10.1016/j.etran.2024.100387.

[34] C. Fabiani, A.L. Pisello, M. Barbanera, L.F. Cabeza, Palm oil-based bio-PCM for energy efficient building applications: multipurpose thermal investigation and life cycle assessment, J. Energy Storage 28 (2020) 101129, https://doi.org/10.1016/j.est.2019.101129.

[35] S. Chen, Z. Wang, P. Zhang, Y. Yu, X. Liu, L. Li, et al., Online core temperature estimation method for lithium-ion batteries over the entire lifecycle, J. Energy Storage 107 (2025) 115033, https://doi.org/10.1016/j.est.2024.115033.

[36] S. Lin, L. Zhou, Research on the performance failure of phase change materials thermal management for lithium battery, Appl. Therm. Eng. 244 (2024) 122743, https://doi.org/10.1016/j.applthermaleng.2024.122743.

[37] M. Ismail, J.R. Panter, S. Landini, Numerical investigation of fin geometries on the effectiveness of passive, phase-change material –based thermal management systems for lithium-ion batteries, Appl. Therm. Eng. 262 (2025) 125216, https://doi.org/10.1016/j.applthermaleng.2024.125216.

[38] S.N. Mishra, S. Sarkar, A. Mukhopadhyay, S. Sen, A lumped electrochemical-thermal model for simulating detection and mitigation of thermal runaway in lithium-ion batteries under different ambient conditions, Therm. Sci. Eng. Prog. 53 (2024) 102764, https://doi.org/10.1016/j.tsep.2024.102764.

[39] C. White, L.G. Swan, Spatial extrapolation of temperature measurements in second-life battery packs using simplified thermal network modelling, J. Energy Storage 112 (2025) 115476, https://doi.org/10.1016/j.est.2025.115476.

[40] E. Paccha-Herrera, W.R. Calderón-Muñoz, M. Orchard, F. Jaramillo, K. Medjaher, Thermal modeling approaches for a licoo2 lithium-ion battery—a comparative study with experimental validation, Batteries 6 (2020) 1–23, https://doi.org/10.3390/batteries6030040.

[41] B.E. Lebrouhi, B. Lamrani, M. Ouassaid, M. Abd-Lefdil, M. Maaroufi, T. Kousksou, Low-cost numerical lumped modelling of lithium-ion battery pack with phase change material and liquid cooling thermal management system, J. Energy Storage 54 (2022) 105293, https://doi.org/10.1016/j.est.2022.105293.

[42] B. Lamrani, B.E. Lebrouhi, Y. Khattari, T. Kousksou, A simplified thermal model for a lithium-ion battery pack with phase change material thermal management system, J. Energy Storage 44 (2021) 103377, https://doi.org/10.1016/j.est.2021.103377.

[43] X. Ke, L. Wang, J. Wang, A. Wang, R. Wang, P. Liu, et al., Battery intelligent temperature warning model with physically-informed attention residual networks, Appl. Energy 388 (2025) 125627, https://doi.org/10.1016/j.apenergy.2025.125627.

[44] S. Li, A.N. Patel, C. Zhang, T. Amietszajew, N. Kirkaldy, G.J. Offer, et al., Internal temperature estimation for lithium-ion batteries through distributed equivalent circuit network model, J. Power Sources 611 (2024) 234701, https://doi.org/10.1016/j.jpowsour.2024.234701.

[45] M. Parhizi, A. Jain, Analytical modeling and optimization of phase change thermal management of a Li-ion battery pack, Appl. Therm. Eng. 148 (2019) 229–237, https://doi.org/10.1016/j.applthermaleng.2018.11.017.

[46] J. Ranjbar Kermani, M. Mahlouji Taheri, M.B. Shafii, A. Moosavi, Analytical solution, optimization and design of a phase change cooling pack for cylindrical lithium-ion batteries, Appl. Therm. Eng. 232 (2023) 120963, https://doi.org/10.1016/j.applthermaleng.2023.120963.

[47] P.M. Tripathi, A.M. Marconnet, Effect of immersion cooling parameters on thermal and electrochemical response of a Li-ion cell, J. Power Sources 632 (2025) 236285, https://doi.org/10.1016/j.jpowsour.2025.236285.

[48] M. Khoshvaght-Aliabadi, P. Ghodrati, Y.T. Kang, Developing a novel battery thermal management system utilizing supercritical CO2 as the cooling medium, Appl. Energy 381 (2025) 125207, https://doi.org/10.1016/j.apenergy.2024.125207.

[49] A. Afass, B. Lamrani, B. Lebrouhi, M.A. Tankari, M. Karkri, S. Landini, et al., Thermal assessment of Li-ion batteries incorporating phase change materials using a new 2D model, Energy Convers. Manag. X 27 (2025) 101051, https://doi.org/10.1016/j.ecmx.2025.101051.

[50] S. Li, N. Kirkaldy, C. Zhang, K. Gopalakrishnan, T. Amietszajew, L.B. Diaz, et al., Optimal cell tab design and cooling strategy for cylindrical lithium-ion batteries, J. Power Sources 492 (2021) 229594, https://doi.org/10.1016/j.jpowsour.2021.229594.

[51] R. Mahamud, C. Park, Spatial-resolution, lumped-capacitance thermal model for cylindrical Li-ion batteries under high Biot number conditions, Appl. Math. Model. 37 (2013) 2787–2801, https://doi.org/10.1016/j.apm.2012.06.023.

[52] Z. Guo, J. Xu, X. Wang, X. Mei, Fast multilayer temperature distribution estimation for lithium-ion battery pack, eTransportation 18 (2023) 100266, https://doi.org/10.1016/j.etran.2023.100266.

[53] J. Shi, H. Zhang, H. Yu, Y. Xu, S. Xu, L. Sheng, et al., Experimental determinations of thermophysical parameters for lithium-ion batteries: a systematic review, eTransportation 20 (2024) 100321, https://doi.org/10.1016/j.etran.2024.100321.

[54] I.D.I.M.M. El, M. Karkri, M. Abdou Tankari, S. Vincent, Hybrid cooling based battery thermal management using composite phase change materials and forced convection, J. Energy Storage 41 (2021) 102946, https://doi.org/10.1016/j.est.2021.102946.

[55] J. Liu, C. Chen, J. Wen, Z. Chang, P.H.L. Notten, Y. Wei, Size effect on the thermal and mechanical performance of cylindrical lithium-ion batteries, Appl. Energy 375 (2024) 124056, https://doi.org/10.1016/j.apenergy.2024.124056.

[56] H. Pegel, D. Wycisk, D.U. Sauer, Influence of cell dimensions and housing material on the energy density and fast-charging performance of tabless cylindrical lithium-ion cells, Energy Storage Mater. 60 (2023) 102796, https://doi.org/10.1016/j.ensm.2023.102796.

[57] J. Gorsch, J. Schneiders, M. Frieges, N. Kisseler, D. Klohs, H. Heimes, et al., Contrasting a BYD Blade prismatic cell and Tesla 4680 cylindrical cell with a teardown analysis of design and performance, Cell Rep. Phys. Sci. 6 (2025), https://doi.org/10.1016/j.xcrp.2025.102453.

[58] F.A. Hamad, E. Egelle, S. Gooneratne, P. Russell, Investigation of the effect of aspect ratio on heat transfer from a heated vertical wall to phase change material in a rectangular enclosure, Therm. Sci. Eng. Prog. 42 (2023) 101865, https://doi.org/10.1016/j.tsep.2023.101865.

[59] P. Saikia, A.S. Azad, D. Rakshit, Thermodynamic analysis of directionally influenced phase change material embedded building walls, Int. J. Therm. Sci. 126 (2018) 105–117, https://doi.org/10.1016/j.ijthermalsci.2017.12.029.

[60] A. Verma, S. Shashidhara, D. Rakshit, A comparative study on battery thermal management using phase change material (PCM), Therm. Sci. Eng. Prog. 11 (2019) 74–83, https://doi.org/10.1016/j.tsep.2019.03.003.

[61] Y. Su, J. Shen, X. Chen, X. Xu, S. Shi, X. Wang, et al., Bio-based eutectic composite phase change materials with enhanced thermal conductivity and excellent shape stabilization for battery thermal management, J. Energy Storage 100 (2024) 113712, https://doi.org/10.1016/j.est.2024.113712.

[62] B. Karami, N. Azimi, S. Ahmadi, Increasing the electrical efficiency and thermal management of a photovoltaic module using expanded graphite (EG)/paraffin-beef tallow-coconut oil composite as phase change material, Renew. Energy 178 (2021) 25–49, https://doi.org/10.1016/j.renene.2021.06.067.

[63] G. Lawer-Yolar, B. Dawson-Andoh, E. Atta-Obeng, Novel phase change materials for thermal energy storage: evaluation of tropical tree fruit oils, Biotechnology Reports 24 (2019) e00359, https://doi.org/10.1016/j.btre.2019.e00359.

[64] Y. He, H. Li, F. Luo, Y. Jin, B. Huang, Q. Qian, Bio-based flexible phase change composite film with high thermal conductivity for thermal energy storage, Compos Part A Appl Sci Manuf 151 (2021) 106638, https://doi.org/10.1016/j.compositesa.2021.106638.

[65] D. Srivastav, N.D. Patil, P.C. Shukla, Bio-based phase change materials for battery thermal management: a numerical investigation for a single Li-ion cell, Appl. Therm. Eng. 278 (2025) 127346, https://doi.org/10.1016/j.applthermaleng.2025.127346.

[66] M. Al-Jethelah, S. Ebadi, K. Venkateshwar, S.H. Tasnim, S. Mahmud, A. Dutta, Charging nanoparticle enhanced bio-based PCM in open cell metallic foams: an experimental investigation, Appl. Therm. Eng. 148 (2019) 1029–1042, https://doi.org/10.1016/j.applthermaleng.2018.11.121.

[67] A.A. Mehrizi, H. Karimi-Maleh, M. Naddafi, F. Karimi, Application of bio-based phase change materials for effective heat management, J. Energy Storage 61 (2023) 106859, https://doi.org/10.1016/j.est.2023.106859.

[68] X. Lin, H.E. Perez, J.B. Siegel, A.G. Stefanopoulou, Y. Li, R.D. Anderson, et al., Online parameterization of lumped thermal dynamics in cylindrical lithium ion batteries for core temperature estimation and health monitoring, IEEE Trans. Control Syst. Technol. 21 (2013) 1745–1755, https://doi.org/10.1109/TCST.2012.2217143.

[69] H. Tu, M. Borah, S. Moura, Y. Wang, H. Fang, Remaining discharge energy prediction for lithium-ion batteries over broad current ranges: a machine learning approach, Appl. Energy 376 (2024) 124086, https://doi.org/10.1016/j.apenergy.2024.124086.

[70] R. Mehta, A. Gupta, Significance of heat of mixing analysed using a pseudo two-dimensional thermo-electrochemical model of lithium-ion cells, Electrochim. Acta 475 (2024) 143509, https://doi.org/10.1016/j.electacta.2023.143509.

[71] A. Nazari, S. Farhad, Heat generation in lithium-ion batteries with different nominal capacities and chemistries, Appl. Therm. Eng. 125 (2017) 1501–1517, https://doi.org/10.1016/j.applthermaleng.2017.07.126.

[72] L.H.J. Raijmakers, D.L. Danilov, R.-A. Eichel, P.H.L. Notten, A review on various temperature-indication methods for Li-ion batteries, Appl. Energy 240 (2019) 918–945, https://doi.org/10.1016/j.apenergy.2019.02.078.

[73] R. Waser, S. Maranda, A. Stamatiou, M. Zaglio, J. Worlitschek, Modeling of solidification including supercooling effects in a fin-tube heat exchanger based latent heat storage, Sol. Energy 200 (2020) 10–21, https://doi.org/10.1016/j.solener.2018.12.020.

[74] A. Halimov, M. Lauster, D. Müller, Validation and integration of a latent heat storage model into building envelopes of a high-order building model for Modelica library AixLib, Energy Build. 202 (2019) 109336, https://doi.org/10.1016/j.enbuild.2019.109336.

[75] I. Medved, A. Trník, L. Vozár, Modeling of heat capacity peaks and enthalpy jumps of phase-change materials used for thermal energy storage, Int. J. Heat Mass Tran. 107 (2017) 123–132, https://doi.org/10.1016/j.ijheatmasstransfer.2016.11.024.

[76] D. Kong, R. Peng, P. Ping, J. Du, G. Chen, J. Wen, A novel battery thermal management system coupling with PCM and optimized controllable liquid cooling for different ambient temperatures, Energy Convers. Manag. 204 (2020) 112280, https://doi.org/10.1016/j.enconman.2019.112280.

[77] S. Xin, C. Wang, H. Xi, Thermal management scheme and optimization of cylindrical lithium-ion battery pack based on air cooling and liquid cooling, Appl. Therm. Eng. 224 (2023) 120100, https://doi.org/10.1016/j.applthermaleng.2023.120100.

[78] A. Al-Masri, K. Khanafer, A. Sedaghat, Passive thermal management of PV solar panels using carbon fiber-enhanced phase change materials: a numerical and optimization study, Int. Commun. Heat Mass Tran. 167 (2025) 109278, https://doi.org/10.1016/j.icheatmasstransfer.2025.109278.

[79] P. Kumar, D. Chaudhary, P. Varshney, U. Varshney, S.M. Yahya, Y. Rafat, Critical review on battery thermal management and role of nanomaterial in heat transfer enhancement for electrical vehicle application, J. Energy Storage 32 (2020) 102003, https://doi.org/10.1016/j.est.2020.102003.

[80] Y. Wang, Y. Zhang, M. Zhang, J. Wang, T. Ma, A novel three-dimensional fast thermal modeling strategy of lithium-ion batteries for online applications, Appl. Therm. Eng. 264 (2025) 125479, https://doi.org/10.1016/j.applthermaleng.2025.125479.

[81] M.A. Alanazi, Experimental estimation of core temperature and directional thermophysical properties for cylindrical lithium-ion battery utilizing an innovative thermal interrogation method, Int. Commun. Heat Mass Tran. 164 (2025) 108827, https://doi.org/10.1016/j.icheatmasstransfer.2025.108827.

[82] S. Kumar, R. Akula, C. Balaji, An inverse methodology to estimate the thermal properties and heat generation of a Li-ion battery, Appl. Therm. Eng. 236 (2024) 121752, https://doi.org/10.1016/j.applthermaleng.2023.121752.

[83] S. Li, M.W. Marzook, C. Zhang, G.J. Offer, M. Marinescu, How to enable large format 4680 cylindrical lithium-ion batteries, Appl. Energy 349 (2023) 121548, https://doi.org/10.1016/j.apenergy.2023.121548.

[84] S. Hong, D. Ma, W. Zeng, J. Shi, Y. Liu, L. Yang, et al., Optimization of fast-charging strategy for LISHEN 4695 cylindrical lithium-ion batteries, J. Power Sources 629 (2025) 236013, https://doi.org/10.1016/j.jpowsour.2024.236013.

[85] T. Waldmann, R.-G. Scurtu, K. Richter, M. Wohlfahrt-Mehrens, 18650 vs. 21700 Li-ion cells – a direct comparison of electrochemical, thermal, and geometrical properties, J. Power Sources 472 (2020) 228614, https://doi.org/10.1016/j.jpowsour.2020.228614.

[86] S. Khange, A.K. Sharma, Elucidating effects of form factors on thermal and aging behavior of cylindrical lithium-ion batteries, Int. J. Therm. Sci. 210 (2025) 109564, https://doi.org/10.1016/j.ijthermalsci.2024.109564.

[87] R.A. Nicholls, M.A. Moghimi, A.L. Griffiths, Influence of latent heat based passive cooling on the performance of EV battery under automotive drive cycles, J. Energy Storage 77 (2024) 109924, https://doi.org/10.1016/j.est.2023.109924.

[88] V. Saxena, S.K. Sahu, S.I. Kundalwal, P.A. Tsai, Enhanced thermal management system for Li-ion batteries using phase change material and liquid cooling under realistic driving cycles, Energy 318 (2025) 134759, https://doi.org/10.1016/j.energy.2025.134759.

[89] A. Afass, B. Lamrani, S. Landini, M.A. Tankari, M. Karkri, T. Kousksou, A comprehensive review of driving cycles for electrical light duty vehicles, in: 2025 International Conference on Clean Electrical Power, ICCEP), 2025, pp. 750–755, https://doi.org/10.1109/ICCEP65222.2025.11143614.

[90] S. Goutam, A. Nikolian, J. Jaguemont, J. Smekens, N. Omar, P. Van Dan Bossche, et al., Three-dimensional electro-thermal model of li-ion pouch cell: analysis and comparison of cell design factors and model assumptions, Appl. Therm. Eng. 126 (2017) 796–808, https://doi.org/10.1016/j.applthermaleng.2017.07.206.

[91] Q. Guo, J. Guo, J. Liu, H. Wang, Effect of thermal management system parameters on the temperature characteristics of the battery module, J. Energy Storage 73 (2023) 108905, https://doi.org/10.1016/j.est.2023.108905.

[92] S. Landini, T.S. O'Donovan, Experimental investigation of lithium-ion cells ageing under isothermal conditions for optimal lifetime performance, J. Energy Storage 48 (2022) 103680, https://doi.org/10.1016/j.est.2021.103680.